Regional aerosol deposition in the human airways: The SimInhale benchmark case and a critical assessment of *in silico* methods

P. Koullapis[a], S. C. Kassinos[a], J. Muela[b], C. Perez-Segarra[b], J. Rigola[b], O. Lehmkuhl[c], Y. Cui[d], M. Sommerfeld[e], J. Elcner[f], M. Jicha[f], I. Saveljic[g], N. Filipovic[g], F. Lizal[f], L. Nicolaou[h,*]

[a]*Department of Mechanical and Manufacturing Engineering, University of Cyprus, Nicosia, Cyprus*
[b]*Heat and Mass Transfer Technological Centre, Universitat Politècnica de Catalunya, Terrassa, Spain*
[c]*Barcelona Supercomputing Center, Barcelona, Spain*
[d]*Chair of Applied Mechanics, Friedrich-Alexander University, Erlangen-Nuremberg, Germany*
[e]*Institute of Process Engineering, Otto von Guericke-University Magdeburg, Halle, Germany*
[f]*Faculty of Mechanical Engineering, Brno University of Technology, Brno, Czech Republic*
[g]*Faculty of Engineering, University of Kragujevac, Kragujevac, Serbia*
[h]*Department of Mechanical Engineering, Imperial College London, London, UK*

Abstract

Regional deposition effects are important in the pulmonary delivery of drugs intended for the topical treatment of respiratory ailments. They also play a critical role in the systemic delivery of drugs with limited lung bioavailability. In recent years, significant improvements in the quality of pulmonary imaging have taken place, however the resolution of current imaging modalities remains inadequate for quantifying regional deposition. Computational Fluid-Particle Dynamics (CFPD) can fill this gap by providing detailed information about regional deposition in the extrathoracic and conducting airways. It is therefore not surprising that the last 15 years have seen an exponential growth in the application of CFPD methods in this area. Survey of the recent literature however, reveals a wide variability in the range of modelling approaches used and in the assumptions made about important physical processes taking place during aerosol inhalation. The purpose of this work is to provide a concise critical review of the computational approaches used to date, and to present a benchmark case for validation of future studies in the upper airways. In the spirit of providing the wider community with a reference for quality assurance of CFPD studies, *in vitro* deposition measurements have been conducted in a human-based model of the upper airways, and several groups within MP1404 SimInhale have computed the same case using a variety of simulation and discretization approaches. Here, we report the results of this collaborative effort and provide a critical discussion of the performance of the various simulation methods. The benchmark case, *in vitro* deposition data and *in silico* results will be published online and made available to the wider community. Particle image velocimetry measurements of the flow, as well as additional numerical results from the community, will be appended to the online database as they become available in the future.

Keywords: inhaled drug delivery, respiratory airways, regional deposition, computational fluid particle dynamics, benchmark case

*Corresponding author at: Department of Mechanical Engineering, Imperial College London, Exhibition Road, London SW7 2AZ, UK. Tel: +44 (0)20 7595 7112.

Email address: laura.nicolaou@imperial.ac.uk (L. Nicolaou)

1. Introduction

Aerosolized delivery of drugs to the lungs is used to treat a number of respiratory diseases, such as asthma, chronic obstructive pulmonary disease (COPD), cystic fibrosis and pulmonary infections. Regional deposition effects play a critical role in applications where targeted drug delivery is needed in order to maximize efficacy and minimize side-effects. Examples include the topical treatment of respiratory diseases, inhaled delivery of chemotherapy agents to lung tumours, and systemic delivery of drugs with limited lung bioavailability. Quantifying regional deposition is therefore important in assessing and optimizing treatment.

Validated computational fluid-particle dynamics (CFPD) methods offer a powerful tool to predict airflow and localized deposition in the respiratory airways, in order to further our understanding of the flow and aerosol dynamics, and test and optimize inhaler therapies. With advances in medical imaging, computational techniques and computing power, there has been an exponential growth in the application of CFPD methods in the respiratory airways over the last 15 years. However, accurate and efficient numerical simulations of the respiratory airways pose a challenge due to the complexities associated with the airway geometry, the flow dynamics and the aerosol physics (Longest and Holbrook, 2012). Numerical studies conducted to date have adopted a variety of computational techniques, a range of airway geometries varying in complexity, and differing assumptions on the flow and aerosol physics. In Section 2, we provide a review of existing methods with particular focus on (i) the airway models adopted; (ii) the solution of the flow field; and (iii) the aerosol physics included in the models. We limit this review to three-dimensional CFPD studies of the exthrathoracic and upper conducting airways. For a broader overview of airflow and particle transport in the human lung the reader is referred to the review papers by Kleinstreuer and Zhang (2010) and Longest and Holbrook (2012).

In addition to the wide variability in the modelling approaches and in the assumptions made about the physical processes that take place during aerosol inhalation, validation of CFPD methods in the respiratory airways is limited. In particular, there is a lack of quantitative validation of localized deposition (Longest and Holbrook, 2012). Most numerical studies have compared total deposition against experimental fits and *in vitro* data in different airway geometries (Zhang et al., 2002; Kleinstreuer and Zhang, 2003; Jayaraju et al., 2007, 2008). It is known, however, that geometric variability has a pronounced effect on aerosol deposition, and in particular on local deposition patterns (Xi and Longest, 2007). A few studies have compared regional deposition results to *in vitro* data in the same geometry, with varying degrees of agreement (Oldham, 2000; Matida et al., 2004; Debhi, 2011). All these studies have focused on either the extrathoracic airways or bifurcation models. The availability of experimental data for validation of local deposition in the tracheobronchial tree proves to be more limited. Therefore, there is a need for improved data sets to better validate computational predictions in local regions of the lungs (Lizal et al., 2015).

Radiological imaging methods can be applied *in vivo* or *in vitro*, in order to obtain deposition measurements for validation. Although *in vivo* measurements play an irreplaceable role as they describe the real state, studies remain limited by the spatial and temporal resolutions of current imaging techniques, and by patient exposure to radiation. *In vitro* methods have the advantage of known geometric characteristics, allowing systematic studies on particle size and flow rate effects (Grgic et al., 2004). Furthermore, they can be performed in the same geometry as the numerical simulation, which allows for direct comparison, and they provide better spatial resolution due to the higher applicable doses of radioactivity.

In this manuscript, we present a benchmark case that can be used for the validation of computational tools intended for regional deposition studies in the upper airways. *In vitro* deposition measurements in a complex realistic geometry are provided at various inhalation flow rates. In

addition, a variety of simulation approaches have been adopted to compute the benchmark case numerically. We present the results for the flow and aerosol deposition, and discuss the performance of the various simulation methods. The purpose of this collaborative work is to (i) provide refined experimental data that can be used for quality assurance of CFPD studies in the upper airways, (ii) provide a critical review of different modelling approaches and (iii) define best practice guidelines where possible.

The benchmark case geometry, experimental data sets, and numerical results will be available online for the wider community. Future work will include particle image velocimetry (PIV) measurements of the flow in order to provide a complete benchmark case for inhaled drug delivery in the upper airways, which has so far been lacking in the literature. Additional numerical results from the community will also be included as they become available. The database will allow for thorough validations of *in silico* models, and will aid in establishing best practice guidelines for predictions of regional deposition in the airways.

The paper is organized as follows: Section 2 provides a review of the current state of the art in numerical modelling of the upper airways. In Section 3, the benchmark case is described in detail. The airway model adopted and the experimental set up for the deposition measurements are presented. In Section 4, the various *in silico* methods employed to compute this case are presented. Results and a comparison of the methods are provided in Section 5. Finally, Section 6 summarizes the work and main findings.

2. Review of *in silico* methods for prediction of aerosol deposition in the upper airways

2.1. Airway models

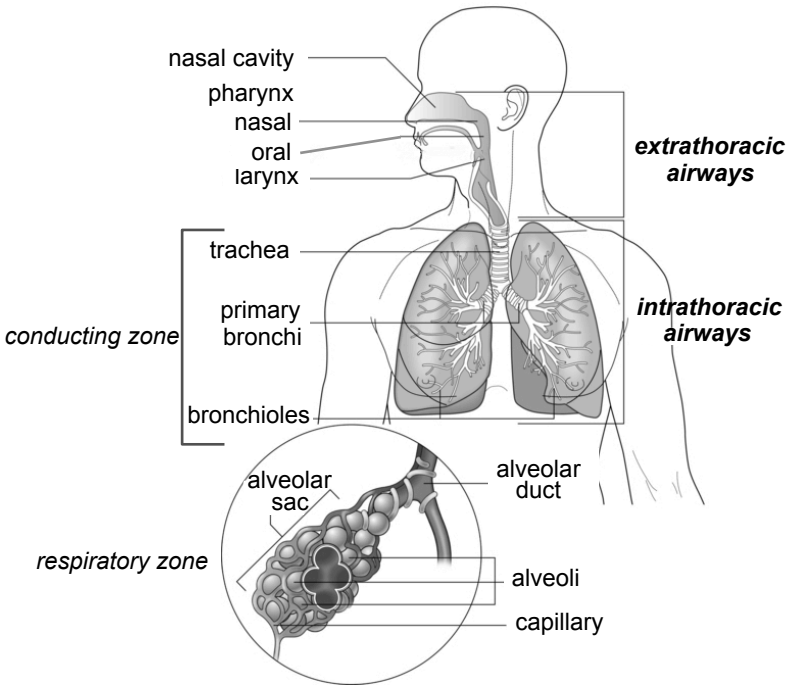

Figure 1: Schematic of the respiratory system, adapted from Thibodeau and Patton (1996).

The respiratory system can be divided into two anatomical areas: the extrathoracic airways consisting of the mouth, nose, pharynx, larynx and trachea; and the intrathoracic airways which begin at the level of the intrathoracic trachea and extend all the way down to the alveoli. The

intrathoracic airways can be further subdivided into the conducting zone (generations 0 to 16), and the respiratory zone where gas exchange takes place (generations 17 to 23). Here, we focus on the extrathoracic and upper conducting airways, which we group together as the 'upper airways'.

Many studies of the upper airways have adopted simplified representations of the airway geometry. Idealized models allow us to elucidate the flow and particle dynamics in the airways without the added complexity of the realistic geometry, and can provide representative estimations of global deposition. For the extrathoracic airways, a number of idealized geometries have been developed, such as the University of Alberta replica, which is representative of a physiologically-averaged adult airway (Stapleton et al., 2000). Built from simple geometric shapes, it nonetheless captures all the basic anatomical features of the real extrathoracic airways and has widely been used in the literature, both in numerical (Matida et al., 2004; Ball et al., 2008; Debhi, 2011; Nicolaou and Zaki, 2016) and *in vitro* studies (DeHaan and Finlay, 2001; Heenan et al., 2003; Grgic et al., 2004; Johnstone et al., 2004). Similarly, Jayaraju et al. (2008) adopted a smoothed geometry based on a representative CT-image chosen among a set of healthy subjects. Others have adopted idealized geometries with variable circular cross-sections based on the hydraulic diameters of a human cast replica (Zhang et al., 2002; Kleinstreuer and Zhang, 2003; Radhakrishnan and Kassinos, 2009; Cui and Gutheil, 2011).

For the tracheobronchial tree, several models have been employed. One of the most commonly used is Weibel's model A, which consists of a fully symmetric tree structure (Weibel, 1963). In reality however, significant variation exists in the geometric parameters for any given generation. More realistic models consist of asymmetric branches with varying lengths, diameters and branching angles (Horsfield et al., 1971; Yeh and Schum, 1980). A number of studies have also been conducted in single and multi-level bifurcations of the tracheobronchial airways (Balásházy and Hofmann, 1993; Balásházy et al., 1999; Zhang et al., 2002; Stylianou et al., 2016).

It is now well understood that geometric variation has a pronounced effect on the flow dynamics and aerosol deposition within the airways (Grgic et al., 2004; Choi et al., 2009; Nicolaou and Zaki, 2013), and that realistic models are required to accurately capture local airflow structures and deposition characteristics (Xi and Longest, 2007). As such, the majority of more recent studies have focused on patient-specific models of the airways (Jayaraju et al., 2007; Lin et al., 2007; Choi et al., 2009; Lambert et al., 2011; Nicolaou and Zaki, 2013; Koullapis et al., 2016). The realistic models are obtained from medical images of the airways, typically via computed tomography (CT) scans or magnetic resonance imaging (MRI), which are then digitally reconstructed via an image registration method. The resulting 3D geometry models, commonly generated as stereolithography (STL) files, can then be meshed for CFPD simulations and used to manufacture casts for *in vitro* studies. Anatomically-accurate models are generally limited to the first 6 or 7 generations due to imaging resolution.

2.2. Flow field

The flow in the upper airways is mostly turbulent and/or transitional in nature, even at low inhalation rates (Dekker, 1961). Therefore, accurate predictions of the flow field require a suitable turbulence model or a sufficiently fine mesh in order to resolve all the scales in the flow. Three different numerical approaches have been adopted in the literature to investigate the airflow in the upper airways: Reynolds-averaged Navier-Stokes (RANS), large eddy simulation (LES), and direct numerical simulation (DNS), listed in increasing level of accuracy and computational cost. In RANS, all turbulent fluctuations are modelled, mainly based on empirical data from canonical flows. In LES, large-scale turbulent structures, or eddies, are numerically resolved while small sub-grid scale structures are modelled by methods similar to RANS. Finally in DNS, all relevant length and time scales are resolved numerically.

The adequacy of standard RANS k-ϵ models for the simulation of flow in the upper airways was discussed by Finlay et al. (1996). Most of these models are designed for high-Reynolds-number flows in simple geometries and are therefore unsuitable for low-Reynolds-number turbulence in complex geometries such as the extrathoracic airways. They are known to perform poorly in flows with recirculating regions, free-shear layers and mean streamline curvature, all of which are present in this region. Stapleton et al. (2000) investigated the suitability of such a model in an idealized mouth and throat geometry, running a laminar and a turbulent case and comparing them to *in vitro* measurements. Whereas the laminar case showed excellent agreement with the experimental data, a large overprediction in deposition was observed in the turbulent case, due to the inadequacy of the turbulence model.

RANS k-ω models have been shown to perform better in the upper airways (Zhang et al., 2002; Matida et al., 2004; Jayaraju et al., 2007; Debhi, 2011). However, large variability in performance exists across studies. Matida et al. (2004) for example, observed a large overprediction in deposition, particularly for smaller particles. The model required the addition of a near-wall correction term in order to reduce the discrepancy with experimental data. Using different k-ω models, Jayaraju et al. (2007) and Zhang et al. (2002) on the other hand, reported better results without the need for a near-wall correction.

Jayaraju et al. (2008) examined the flow in a simplified human mouth-throat model using both RANS k-ω and LES methods. Their comparison showed that the LES velocity and kinetic energy profiles were in good agreement with experimental data, as opposed to those from RANS. Mouth-throat deposition was also simulated for particle sizes ranging from 2-10 μm. While the k-ω and LES simulations produced similarly good predictions for bigger particles, RANS overpredicted deposition for particle sizes below 5μm. Since the upper limit of the respirable range for inhalation drugs is typically 5μm, the authors concluded that LES would be the preferred method for predicting aerosol deposition in the upper airways.

Due to the high computational demands of DNS, only a few studies have adopted this approach for the upper airways. Lin et al. (2007) compared the flow in a realistic geometry of the intrathoracic airways, with and without the mouth-throat region, in order to assess the effect of the laryngeal jet on airflow characteristics. Their study revealed that turbulence induced by the laryngeal jet can significantly affect the flow patterns as well as the tracheal wall shear stress, and they concluded that subject-specific evaluations should include the extrathoracic airways.

Ball et al. (2008) adopted a lattice Boltzmann method (LBM) to conduct a direct numerical simulation of the flow inside an idealized model of the extrathoracic airways. Results were compared to hot-wire measurements performed in the same model. The LBM calculations were shown to yield better results than RANS, and reproduced significant detail of the experimentally observed flow features.

Nicolaou and Zaki (2013) performed DNS in a set of realistic mouth-throat geometries, using an immersed boundary method (Nicolaou et al., 2015). The authors reported that geometric variation, even within the same subject, has a large impact on both the mean flow and the turbulent fluctuations. Their study also provided a physical explanation for the dependence of deposition on the flow Reynolds number. The empirical Stokes-Reynolds number correlation, $StkRe^{0.37}$, typically adopted to report extrathoracic deposition was related theoretically to the dimensionless particle relaxation time, and was shown to arise due to the fact that deposition in the mouth-throat region occurs via both impaction and turbulent diffusion.

2.3. Aerosol transport and deposition

Aerosol deposition in the upper airways occurs primarily via impaction, due to the high velocities and rapid changes in flow direction. The inertia of the particles causes them to deviate

from the fluid streamlines and collide with the airway walls. The larger the particles, the higher the probability of deposition by impaction. Turbulent dispersion also plays a role in this region, in particular for small particles whose trajectories are considerably influenced by the fluctuations in the flow.

Particle transport can be modelled using an Eulerian or a Lagrangian approach. The Eulerian, or two-fluid, approach treats the dispersed phase as a continuum, solving the conservation equations of particle mass and momentum. On the other hand, the Lagrangian approach treats the dispersed phase as a set of individual point-particles in a continuous carrier phase. The particles are tracked through the flow field by solving the equations of motion for each particle with the relevant forces acting on it. Description of turbulent dispersion and collision of particles with the airway walls is more natural with this approach. For this reason, the Lagrangian approach has featured prominently in studies of aerosol deposition in the airways (Kleinstreuer and Zhang, 2003; Matida et al., 2004; Jayaraju et al., 2007; Li et al., 2007; Radhakrishnan and Kassinos, 2009; Debhi, 2011; Koullapis et al., 2016; Nicolaou and Zaki, 2016).

In all these studies, the particles are assumed to be spherical, non-rotating and non-interacting. The aerosol is considered a dilute suspension and modelled using a one-way coupling approach, where the effect of the particles on the flow and inter-particle interactions are neglected. In reality however, inhaled particles are often non-spherical (e.g. dry powder inhaler formulations), and may possibly collide with each other and aggregate.

The equations of motion that describe the change in position, $\boldsymbol{x}_p$, and velocity, $\boldsymbol{u}_p$, along the particle trajectory are given by

$$\frac{d\boldsymbol{x}_p}{dt} = \boldsymbol{u}_p, \tag{1}$$

$$m_p \frac{d\boldsymbol{u}_p}{dt} = \sum \boldsymbol{F}, \tag{2}$$

where m_p is the mass of the particle and $\sum \boldsymbol{F}$ represents all the forces acting on it. The balance of forces acting on particles as they travel in a fluid was derived from first principles by Maxey and Riley (1983) in the low Reynolds number limit, and is given by

$$\begin{aligned} m_p \frac{d\boldsymbol{u}_p}{dt} = & \underbrace{\frac{18\mu_f}{\rho_p d_p^2} m_p \left(\boldsymbol{u}_f - \boldsymbol{u}_p\right)}_{\text{drag force}} + \underbrace{m_f \left(\frac{D\boldsymbol{u}_f}{Dt}\right)}_{\text{pressure gradient force}} + \underbrace{\frac{1}{2} m_f \left(\frac{D\boldsymbol{u}_f}{Dt} - \frac{d\boldsymbol{u}_p}{dt}\right)}_{\text{added mass force}} \\ & + \underbrace{\frac{3}{2} d_p^2 \left(\pi \rho_f \mu_f\right)^{\frac{1}{2}} \int_{t_0}^{t} \frac{\frac{d}{dt'}\left(\boldsymbol{u}_f - \boldsymbol{u}_p\right)}{(t-t')^{\frac{1}{2}}} dt'}_{\text{Basset history force}} + \underbrace{\boldsymbol{g}\left(m_p - m_f\right)}_{\text{gravity force}}. \end{aligned} \tag{3}$$

Here d_p and ρ_p are the particle diameter and density respectively, μ_f and ρ_f are the dynamic viscosity and density of the fluid, $\boldsymbol{u}_f$ is the fluid velocity at the particle location, and m_f is the mass of fluid displaced by the particle.

Equation 3 does not include inertial effects, such as form drag or lift force, and is therefore only valid for small particle Reynolds numbers, $Re_p < 1$, where

$$Re_p = \frac{\rho_f d_p |\boldsymbol{u}_f - \boldsymbol{u}_p|}{\mu_f}. \tag{4}$$

At higher Reynolds numbers, the drag force is given by

$$\boldsymbol{F}_D = \frac{18\mu_f}{\rho_p d_p^2} m_p \left(\boldsymbol{u}_f - \boldsymbol{u}_p\right) \frac{C_D Re_p}{24}, \tag{5}$$

where C_D is the drag coefficient, which takes into account both skin friction and form drag, and depends on the particle Reynolds number. Many empirical and semi-empirical equations have been proposed to approximate the drag coefficient over different particle Reynolds number ranges. For aerosol particles in the respiratory airways, the correlation proposed by Schiller and Naumann (1935), which is valid for $Re_p < 800$, is commonly adopted:

$$C_D = \frac{24}{Re_p}\left(1 + 0.15Re_p^{0.687}\right). \tag{6}$$

For particles of comparable size to the mean free path of the fluid molecules, rarefaction effects become significant and the fluid can no longer be treated as a continuum. In order to account for slip at the particle surface due to non-continuum effects, a correction factor is often applied to the drag. A correlation for the Cunningham correction factor for airborne particles was derived by Davies (1945), and is given by

$$C_C = 1 + \frac{2\lambda}{d_p}\left(1.257 + 0.4\exp\left(-\frac{1.1d_p}{2\lambda}\right)\right), \tag{7}$$

where $\lambda = 0.070\mu$m is the mean free path of air. For 1μm particles at standard conditions, drag is 15% lower than that predicted without taking into account the slip correction. As particle size decreases beyond 1μm, slip rapidly increases.

In shear flow, particles may experience a transverse lift force. This force, known as Saffman lift, has been shown to be most prominent for large particles and small particle-to-fluid density ratios, ρ_p/ρ_f (Kallio and Reeks, 1989; Young and Leeming, 1997). For aerosol particles in turbulent channel flow, McLaughlin (1989) found that the Saffman lift force had virtually no effect on particle trajectories, except within the viscous sublayer, where it played a significant role both in the inertial deposition and in the accumulation of particles.

Submicrometer particles are also subjected to Brownian motion, caused by random collisions with the gas molecules (Ounis et al., 1991). The Brownian force can be modelled as a Gaussian white-noise random process (Li and Ahmadi, 1992). Li and Ahmadi (1992) studied the effects of Brownian diffusion on particle dispersion and deposition in turbulent channel flow. Very near the wall, where turbulent fluctuations die down, Brownian motion was shown to be the dominant mechanism for diffusion of particles smaller than 0.1μm. For particles larger than 0.5μm, the effect of Brownian diffusion was negligibly small.

The majority of studies focused on micron-sized particles in the upper airways have taken into account the drag and gravitational force, and discounted all other forces acting on the particles (Matida et al., 2004; Jayaraju et al., 2007; Debhi, 2011; Lambert et al., 2011; Nicolaou and Zaki, 2016). A couple of studies have considered only the aerodynamic drag, based on order-of-magnitude arguments (Zhang et al., 2002; Kleinstreuer and Zhang, 2003; Li et al., 2007). Simulations with and without the gravitational force were performed by Ma and Lutchen (2009) at an inhalation flow rate of 15 L/min. When gravity was ignored, there was a maximum 10% reduction in total deposition which showed that, while inertial impaction is the dominant deposition mechanism for micron-sized particles in the upper airways, gravitational sedimentation is also important and should be taken into account. The effect of gravity is more significant for larger particles, and diminishes as the flow rate increases. Due to the large particle-to-fluid density ratios for aerosol particles in air, the Saffman lift, pressure gradient, added mass, and Basset forces are typically considered insignificant in the upper airways (Finlay et al., 1996).

Other effects on aerosol transport and deposition in the airways such as humidity, temperature and electrostatic charge are less understood. Vaporisation as well as particle growth due to hygroscopicity can both occur in the airways. Zhang et al. (2004) examined fuel droplet deposition

in an upper airway model, with and without evaporation. Their results demonstrated that thermal effects were significant in the oral airways at low inhalation rates (Q = 15 L/min). Evaporation increased with higher ambient temperatures and lower inspiratory flow rates, resulting in lower deposition fractions. Longest and Xi (2008) evaluated the effect of condensation particle growth on the transport and deposition of cigarette smoke particles in the upper respiratory tract, under various relative humidity and temperature conditions. For the inhalation of warm saturated air 3°C above body temperature, 200 and 400 nm particles were observed to increase in size to above 3µm near the trachea inlet, leading to an increase in deposition compared to the non-hygroscopic case.

Recently, Koullapis et al. (2016) investigated the effect of electrostatic charge on aerosol deposition in a realistic geometry of the upper airways. Electrostatic charge was shown to increase deposition of smaller particles by as much as sevenfold, with most of the increase located in the mouth-throat region. The impact of inhalation flow rate on the deposition of charged particles was negligible for sizes smaller than 1µm, whereas inertial impaction prevailed over electrostatic deposition for particles above 2.5µm, with deposition increasing as flow rate increased. Overall, the authors reported a significant interplay between particle size, electrostatic charge, and flow rate.

3. Benchmark case

3.1. Airway geometry

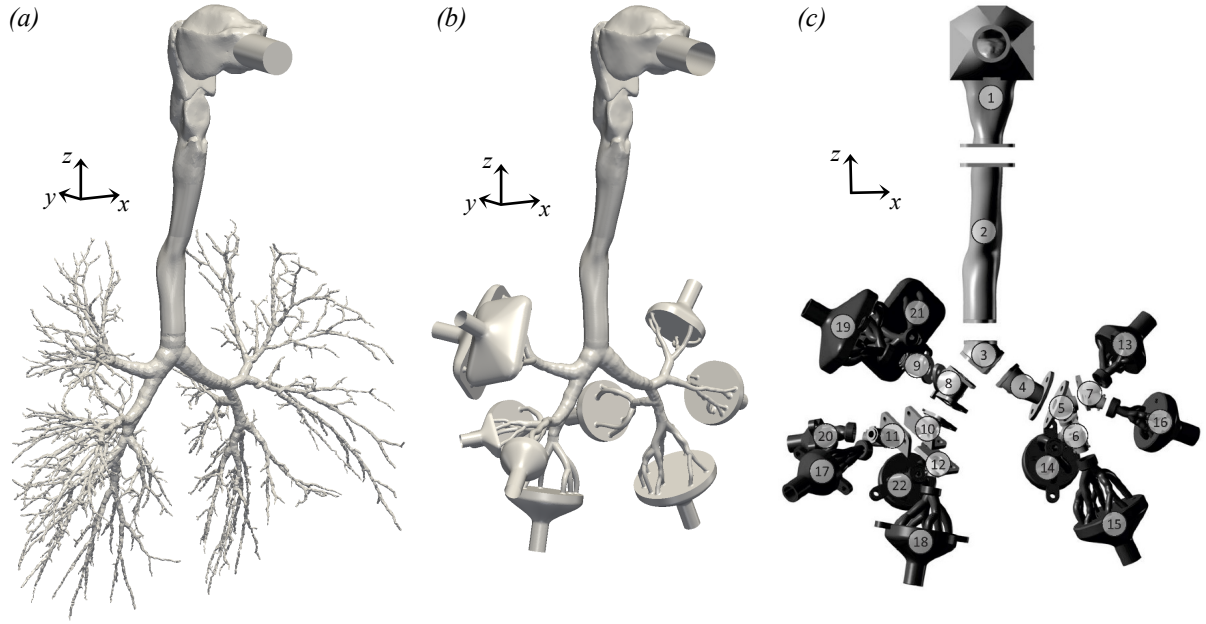

Figure 2: Geometry of the respiratory airways: (*a*) original realistic airway geometry; (*b*) geometry adopted for the benchmark case; (*c*) physical segmented model for deposition measurements.

The realistic airway geometry used to construct the benchmark case model is shown in figure 2*a*. It comprises of the oral cavity, larynx and tracheobronchial airways down to the 12th generation of branching. The tracheobronchial tree was acquired from a human lung of an adult male, excised at autopsy and fixed with a liquid rubber solution at nearly end-inspiratory volume. The lung tissue was removed and the rubber cast of the bronchial tree was scanned using high-resolution computed tomography (HRCT) (Schmidt et al., 2004). The extrathoracic airways were obtained from the Lovelace Respiratory Research Institute (LRRI) upper airway model. The oral

cavity was moulded from an *in vivo* dental impression of a Caucasian male at approximately 50% of the full opening, and the remaining of the model was acquired from a cadaver (Cheng et al., 1997). The LRRI geometry was obtained as a wax cast, which was scanned by an Atos (GOM, Braunschweig, Germany) device, converted to STL format, and concatenated with the bronchial tree model at the trachea. Further details on the construction of the airway model can be found in Lizal et al. (2012).

Figure 2*b* shows the geometry employed in the *in vitro* experiments and numerical simulations. Only branches with diameter above 3mm were used, and the terminal bronchi segments were connected to 10 outlets. The physical model for deposition measurements was produced by stereolithography (Lizal et al., 2015). A 3mm-thick envelope was created around the original geometry to obtain a negative cast of the airways. The model was divided into sections to facilitate the measurement of regional deposition by various methods, such as optical microscopy and gravimetry (figure 2*c*).

3.2. Deposition measurements

Measurement of the regional aerosol deposition was performed by positron emission tomography (PET). Aerosol particles of di-2-ethyl hexyl sebacate (DEHS) were generated using a Condensation Monodisperse Aerosol Generator, and radiolabeled with Fluorine 18. The aerosol was fed through a 85Kr-based NEKR-10 charge equilibrator to reduce the electrostatic deposition of particles, and the size and concentration of the particles was monitored by a PAM aerosol monitor throughout the experiment. A schematic of the experimental set up is shown in figure 3.

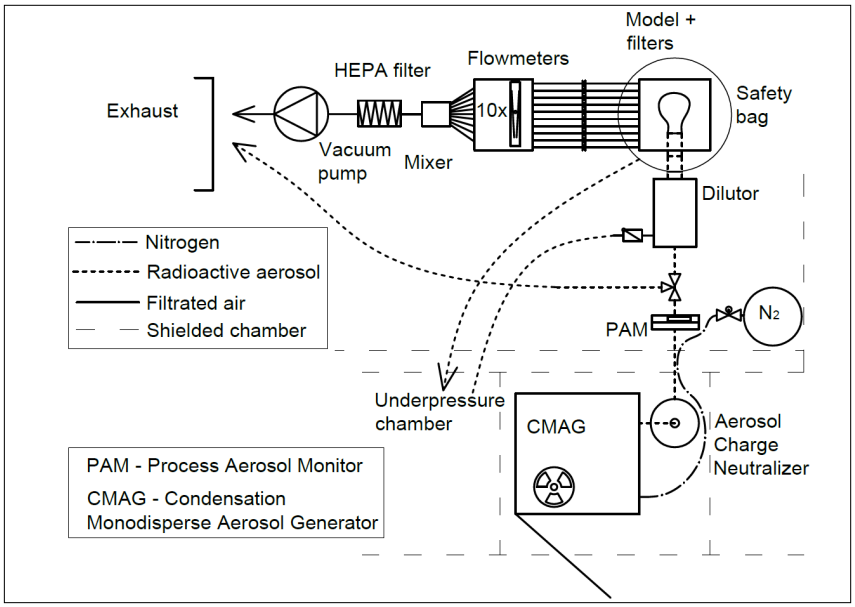

Figure 3: Schematic of the experimental set up for deposition measurements in the airways. Reprinted from Lizal et al. (2015) by permission of SAGE Publications.

The experiments were performed at steady-state inhalation with flow rates of 15, 30 and 60 L/min. The total duration of inhalation was between 10 to 15 minutes. Two sizes of particles were measured with mass median aerodynamic diameter of 2.5 and 4.3µm. The standard geometric deviation of size was smaller than 1.24. Particles that did not deposit in the model were collected on filters downstream of each of the ten output branches. Following exposure, CT and PET images were obtained in a PET-CT scanner, and used to evaluate deposition in each segment of the model

based on a volume radioactivity analysis. A detailed description of the method is provided by Lizal et al. (2015).

4. Numerical methods

Six different groups have performed simulations of the flow and particle deposition in the benchmark case airway geometry. A general description of the experiments was provided, but the groups were left free to adopt their preferred methodologies, in order to obtain an indication of the degree of variability in numerical approaches. The results presented here correspond to the 60 L/min case, however *in silico* and *in vitro* results at Q ={15, 30} L/min will also be provided online. A summary of the methods adopted to solve the flow field and the particle transport is given below.

4.1. Flow field

Different discretization techniques, namely finite volume and finite element methods, were employed in the various simulations to solve the governing equations for the flow. In order to model the turbulence in the airways, three different LES and three steady-state RANS models were adopted. The governing flow equations are given by,

$$\frac{\partial u_i}{\partial t} + u_j \frac{\partial u_i}{\partial x_j} = -\frac{1}{\rho}\frac{\partial p}{\partial x_i} + \frac{\partial}{\partial x_j}\left[(\nu + \nu_T)\frac{\partial u_i}{\partial x_j}\right], \tag{8}$$

$$\frac{\partial u_j}{\partial x_j} = 0, \tag{9}$$

where u_i are the velocity components, p is the pressure, ρ and ν are the density and kinematic viscosity of the fluid respectively, and ν_T is the turbulent viscosity. In the LES simulations, $\boldsymbol{u}$ and p represent the filtered velocity and pressure, respectively. In RANS, these correspond to time-averaged variables.

The Reynolds number at the inlet, based on the inflow bulk velocity and inlet tube diameter, is $Re = \frac{U_{in}D_{in}}{\nu} = 3745$, which lies in the turbulent regime. In order to generate turbulent inflow conditions, a mapped inlet, or recycling, boundary condition was used in simulations LES1 and LES2 (Tabor and Baba-Ahmadi, 2010). To apply this boundary condition, the pipe section at the inlet was extended and initially fed with an instantaneous turbulent velocity field generated in a separate pipe flow LES. During the simulation of the airway geometries, a scaled mapping of the velocity field from the midplane of the extended pipe was applied at the inlet to the mouth. In RANS1, the time-averaged velocity field and turbulent variables from a precursor pipe simulation were applied at the inlet. Simulation LES3 specified a pressure boundary condition and extrapolated the velocities at the inlet, and RANS2 and RANS3 applied uniform velocity. At the outlets, flow rates were prescribed according to those observed *in vitro*.

Unstructured body-fitted meshes were employed, ranging from 1.3 million grid cells (RANS3) to 50 million (LES1). The fine-grid LES simulation, LES1, is adopted as the reference case. Table 1 below summarizes the computational details for each method. In addition to the cases shown in table 1, a coarse LES1 simulation, LES1c, was also performed, in order to assess the effect of grid size on flow and deposition. In this simulation, the LES3 mesh consisting of 7 million cells, and a time step of 1e-5s were employed. All other parameters remained the same as in LES1.

A comparison of the mean flow and turbulence statistics across the six methods is provided in Section 5.1. In RANS, the mean velocity, $\bar{\boldsymbol{u}}$, and mean turbulent kinetic energy per unit mass, k,

are obtained directly from the time-averaged Navier-Stokes and turbulence closure equations. In the LES simulations, the mean velocities and resolved root-mean-square fluctuations, $\boldsymbol{u}_{rms}$, were computed with a running average in time:

$$\bar{\boldsymbol{u}} = \frac{1}{T}\int_0^T \boldsymbol{u}\, dt, \tag{10}$$

$$\boldsymbol{u}_{rms} = \left(\overline{\boldsymbol{u}'^2}\right)^{1/2} = \left(\frac{1}{T}\int_0^T \boldsymbol{u}^2\, dt - \bar{\boldsymbol{u}}^2\right)^{1/2}, \tag{11}$$

where T is the time period over which statistics were collected. The resolved turbulent kinetic energy is given by $k = \frac{1}{2}\overline{u_i' u_i'}$.

Table 1: Computational details of the in silico methods used to solve the flow in the airways.

	LES1	LES2	LES3	RANS1	RANS2	RANS3
Flow solver	OpenFoam (FVM)	Termofluids (FVM)	Alya (FEM) (Vázquez et al., 2016)	OpenFoam (FVM)	CD-Adapco Star-CCM+ (FVM)	PAKF solver (FEM)
Turbulence model	LES dynamic Smagorinsky (Lilly, 1992)	LES variational multiscale (Hughes et al., 2000)	LES WALE (Nicoud and Ducros, 1999)	RANS k-ω-SST (Menter, 1994)	RANS low-Re k-ω-SST (Menter, 1994)	RANS k-ϵ model (Launder and Spalding, 1974)
Inlet boundary conditions	atmospheric pressure, turbulent (mapped inlet)	atmospheric pressure, turbulent (mapped inlet)	atmospheric pressure, extrapolated velocity	atmospheric pressure, turbulent inlet	atmospheric pressure, uniform velocity	atmospheric pressure, uniform velocity
Outlet boundary conditions	zero-gradient pressure, specified flow rates	zero-gradient pressure, specified flow rates	zero-gradient pressure, specified flow rates	zero-gradient pressure, specified flow rates	zero-gradient pressure, specified flow rates	zero-gradient pressure, specified flow rates
Mesh size	50M	10M	7M	12M	6.3M	1.3M
Mesh type	tetrahedral, 3-5 wall prism layers	tetrahedral, 3 wall prism layers	tetrahedral, 3 wall prism layers	tetrahedral, no wall prism layers	polyhedral, 8 wall prism layers	tetrahedral, no wall prism layers
Time step	2.5e-6s	4.55e-7s	1.3e-5s	1e-5s	2.5e-4s	1e-5s

4.2. Particle tracking

To model the aerosol transport and deposition in the airways, all simulations employed a Lagrangian particle-tracking approach and assumed one-way coupling between the flow and the particles. Different particle-tracking algorithms were adopted, which differ in the integration schemes used to solve the particle equations of motion, and in the interpolation methods used to determine the fluid velocity at the particle position. The approaches also differ in the forces acting on the particles. Aerodynamic drag, which is the dominant force on micron-sized particles in the upper airways, was included in all simulations. The effect of gravity was also taken into account in all but one of the cases, and simulations LES1 and LES2 included Brownian motion. The Cunningham correction factor (equation 7) was applied in LES1, LES2 and RANS1.

The particle equations of motion are given by

$$m_p \frac{d\boldsymbol{u}_p}{dt} = \frac{3}{4}\frac{\rho_f}{\rho_p}\frac{m_p}{d_p}\frac{C_D}{C_C}|\boldsymbol{u}_f - \boldsymbol{u}_p|\left(\boldsymbol{u}_f - \boldsymbol{u}_p\right) + m_p\boldsymbol{g}\frac{\rho_p - \rho_f}{\rho_p} + \boldsymbol{F}_B, \tag{12}$$

where the first and second terms on the right-hand side are the drag and gravitational forces respectively, and $\boldsymbol{F}_B$ represents the Brownian force included in LES1 and LES2. The amplitudes of the Brownian force components at time t are evaluated from

$$F_{B_i} = G_i\sqrt{\frac{2k_B^2T^2}{\tilde{D}\Delta t}}, \tag{13}$$

where G_i is a zero mean variant from a Gaussian probability density function, $T = 310$ K is the absolute temperature, $\tilde{D} = (k_BTC_C)/(3\pi\mu_f d_p)$ is the Brownian diffusivity, $k_B = 1.3806488 \times 10^{23}$ J/K is the Boltzmann constant, and Δt is the time step used in the integration of the particle equations of motion (Ounis et al., 1991).

In the RANS simulations, where only mean velocities are computed, a turbulent dispersion model is required in order to take into account the effect of the velocity fluctuations on the particles. RANS1 adopted a continuous random walk technique, where the fluctuating velocities are obtained from the generalized Langevin equation (Sommerfeld et al., 1993). In RANS2, an eddy interaction model was applied (Gosman and Ioannides, 1983). This approach assumes isotropic turbulence and generates random fluctuations from a Gaussian distribution of zero mean and $2k/3$ variance, where k is the turbulent kinetic energy. Particles interact with an eddy until either the lifetime of the eddy is over or the particle crosses the eddy, after which interaction with a new eddy begins. RANS3 performed mean-flow tracking, without any turbulent dispersion model. In the LES simulations, the resolved velocity field includes the large-scale fluctuations, but subgrid-scale particle dispersion was not included.

Deposition was assumed once a particle comes into contact with the airway walls. Reflection and re-suspension were not included, since the *in vitro* experiments used liquid particles which deposit when they hit the surface of the cast. *In vivo*, the existence of a mucus layer on the inner walls of the airways ensures that particles colliding with the surface deposit.

The particle diameters ranged from $d_p = 0.5\mu$m to 10μm, and the particle density was set to $\rho_p = 914$ kg/m^3, which corresponds to di-ethylhexyl sebacate (DEHS) particles in air at room temperature. Particles were distributed uniformly across the inlet, but the total number of particles injected into the flow and their release period varied across simulations. Details of the particle-tracking schemes adopted are provided in table 2.

It is interesting to see how, for the same case, user specification varies widely. In particular, the boundary conditions for the flow, choice of forces acting on the particles, and release time and number of particles differ across simulations. In addition to serving as a validation case for computational models of flow and aerosol deposition in the upper airways, this benchmark case allows us to examine the sensitivity of predictions to the numerical methods adopted and the assumptions made in the modelling, and to identify best practice guidelines. In the following section, we examine the flow and particle deposition obtained using the different computational approaches, and comment on the variability of results.

Table 2: Computational details of the Lagrangian particle-tracking schemes.

	LES1	LES2	LES3 (Houzeaux et al., 2016)	RANS1	RANS2	RANS3
Time integration scheme	implicit Euler	explicit second-order	(implicit) Newmark	implicit Euler	implicit Euler	(implicit) trapezoidal
Forces on particles	drag, gravity, Brownian	drag, gravity, Brownian	drag, gravity	drag, gravity (Brownian, lift)	drag	drag, gravity
Drag coefficient (C_D)	Schiller and Naumann (1935)	Schiller and Naumann (1935)	Ganser (1993)	Schiller and Naumann (1935)	Schiller and Naumann (1935)	Morsi and Alexander (1972)
Cunningham correction factor (C_C)	Davies (1945)	Davies (1945)	1.0	Davies (1945)	1.0	1.0
Turbulent dispersion	———	———	———	continuous random walk	eddy interaction model	mean-flow tracking
Number of particles per size	100,000	100,000	300,000	100,000	10,000	30,000
Release time of particles	0.025s	0.025s	0.3s	0.025s	0.1s	0.08s

5. Results and discussion

5.1. Air flow

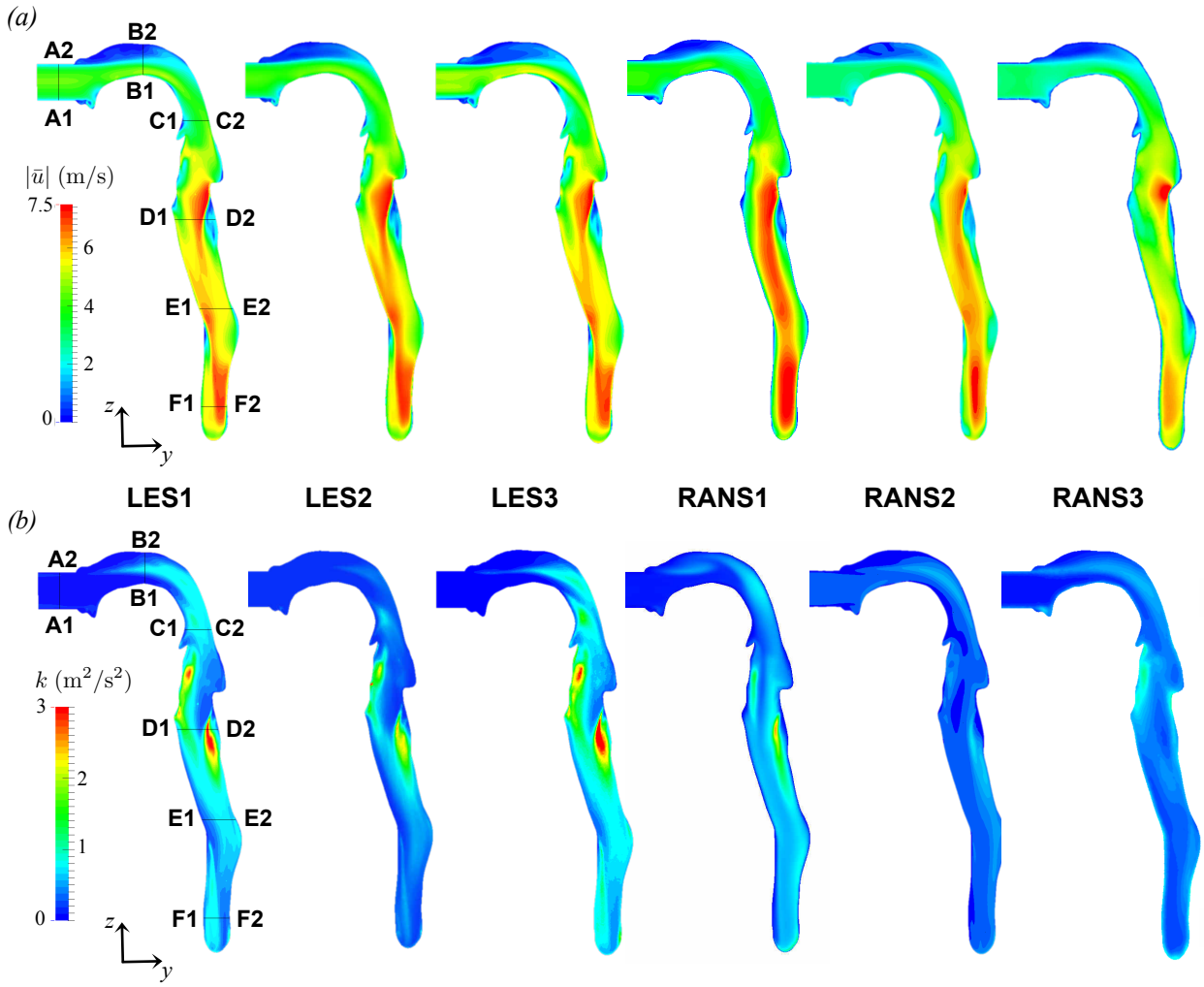

Figure 4: Contours of mean velocity magnitude and turbulent kinetic energy in the central sagittal plane of the extrathoracic airways and trachea.

Figure 4*a* shows contours of the mean velocity magnitude in the central sagittal plane of the extrathoracic airways and the trachea, obtained using the six different numerical methods. Profiles at various cross-sections are also plotted in figure 5 for a more detailed comparison. Velocities are generally low in the mouth (B1-B2) and pharynx (C1-C2), and a large separated region is observed along the upper wall of the oral cavity (B1-B2). As a result of the glottal constriction, the flow accelerates in the larynx and a separated shear layer develops at the level of the vocal cords due to the airway curvature (D1-D2). In most simulations, a recirculation region is observed near the posterior wall of the trachea, behind the separated shear layer (D1-D2). Further downstream, a bend in the trachea (E1-E2) causes the high-speed velocity to shift from the anterior to the posterior wall (F1-F2), and leads to the formation of a small region of separation at the anterior wall, which is visible in the LES and RANS2 simulations.

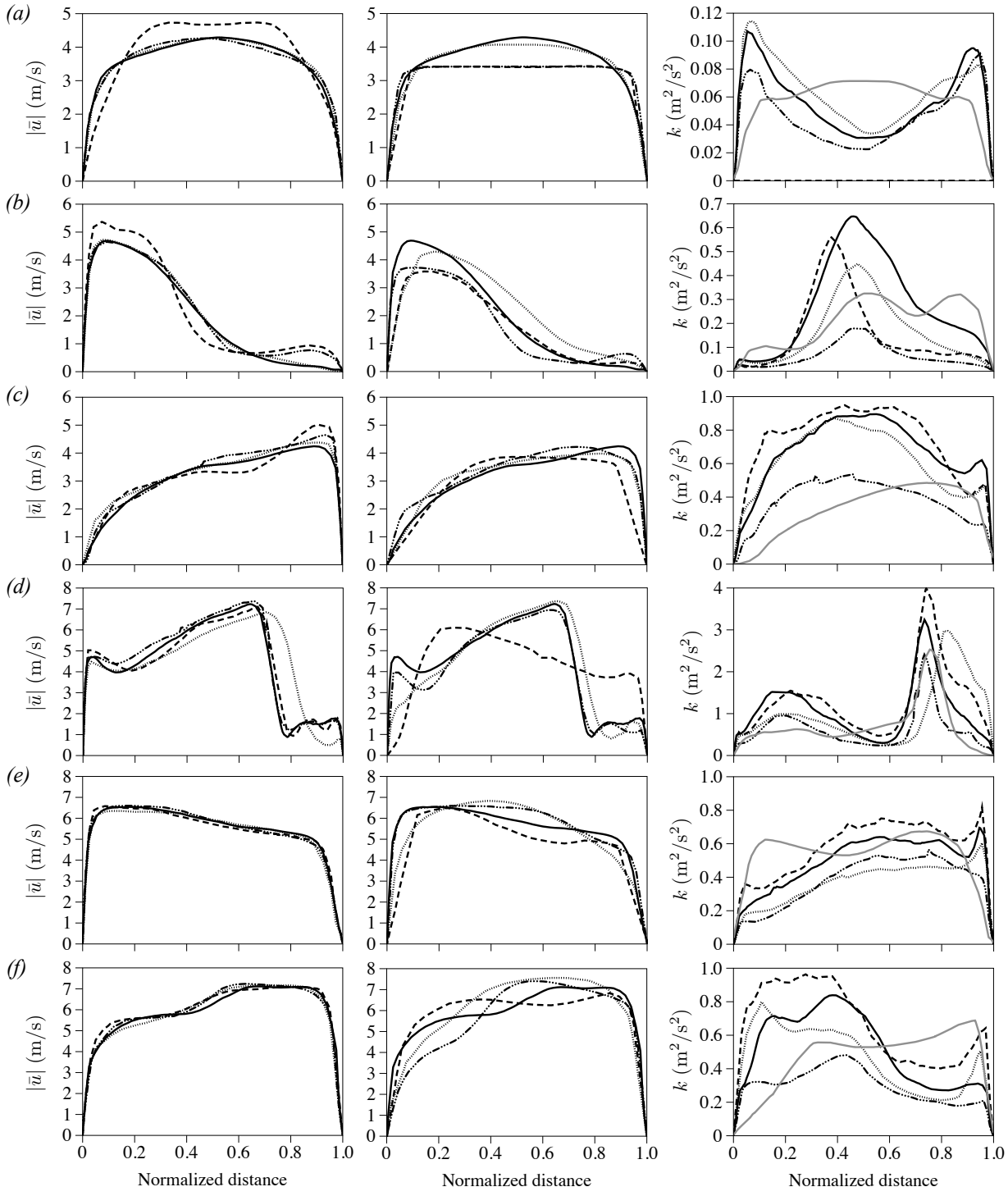

Figure 5: Profiles of mean velocity magnitude and turbulent kinetic energy at various cross-sections of the extrathoracic airways and trachea: (*a*) A1-A2; (*b*) B1-B2; (*c*) C1-C2; (*d*) D1-D2; (*e*) E1-E2; and (*f*) F1-F2. On the left: LES results for mean velocity, — LES1, ····· LES1c, -·-·- LES2, - - - LES3; middle: RANS results for mean velocity, — LES1, ····· RANS1, -·-·- RANS2, - - -RANS3; and right: LES results for turbulent kinetic energy, — LES1, ····· LES1c, -·-·- LES2, - - - LES3, — RANS1.

Good qualitative agreement in the mean flow fields is seen across LES simulations. The biggest differences are observed in regions of recirculating flow (B1-B2 and D1-D2). Higher peak velocities are predicted by LES3 in the mouth (B1-B2) and upper pharynx (C1-C2), which can be attributed to the different inflow conditions applied in this simulation. Velocities were extrapolated at the inlet, as opposed to specifying turbulent inflow conditions, resulting in higher velocity in the inlet pipe (A1-A2). The variations in the mean flow due to inflow conditions die out in the larynx, and very good agreement in the velocity profiles is observed downstream (figures 5*d*-*f*).

Larger discrepancies in the results are observed in the RANS calculations. In particular, the RANS simulations have more difficulty predicting the separated shear layer in the larynx, and the recirculation regions. The low-*Re* k-ω model with prism layer mesh at the wall (RANS2) is in closer agreement to the LES results, whereas the k-ϵ model (RANS3) displays the largest differences. The discrepancies observed in the RANS3 simulation are likely due to both the low grid resolution as well as the use of a k-ϵ turbulence model. Standard k-ϵ models are typically designed for high-Reynolds-number flows in simple geometries, and are known to perform poorly in flows with recirculating regions, free-shear layers and mean streamline curvature, all of which are present in the extrathoracic airways (Finlay et al., 1996).

Contours of the mean turbulent kinetic energy, k, in the extrathoracic airways and trachea are shown in figure 4*b*. Turbulent kinetic energy levels are low at the inlet, and start to increase towards the back of the mouth and the upper pharynx. The maximum kinetic energy occurs in the larynx, near the anterior wall (downstream of C1-C2), and in the trachea, near the edge of the separated shear layer (D1-D2). It is evident that RANS2 and RANS3 are highly dissipative, and significantly underpredict turbulence levels in the airways. We therefore limit the following turbulent kinetic energy results to those obtained by the LES methods and RANS1.

Profiles of the turbulent kinetic energy at various cross-sections of the airways are shown in figure 5. Larger discrepancies across simulations are observed in the turbulence characteristics, compared to the mean flow field. Despite similar turbulence intensities at the inlet between LES1 and LES2, LES2 generally underpredicts turbulence levels inside the airways. Slightly lower TKE levels are also observed in LES1c. In LES3, although turbulent inflow conditions were not prescribed, the flow transitions to turbulence at the back of the mouth (B1-B2). Similar flow development has also been observed in other patient-specific airway geometries under laminar inflow conditions (Nicolaou and Zaki, 2013). Downstream of the mouth, a fairly good agreement exists in the turbulence levels between LES1 and LES3. Note that simulations LES1c, LES2 and LES3 were conducted on similar mesh sizes, which suggests that the lower turbulent kinetic energy levels observed in LES1c and LES2 are due to more dissipative turbulence models or discretization schemes. The predictions obtained by RANS1 are in global fair agreement, but fail to capture the local maxima and minima.

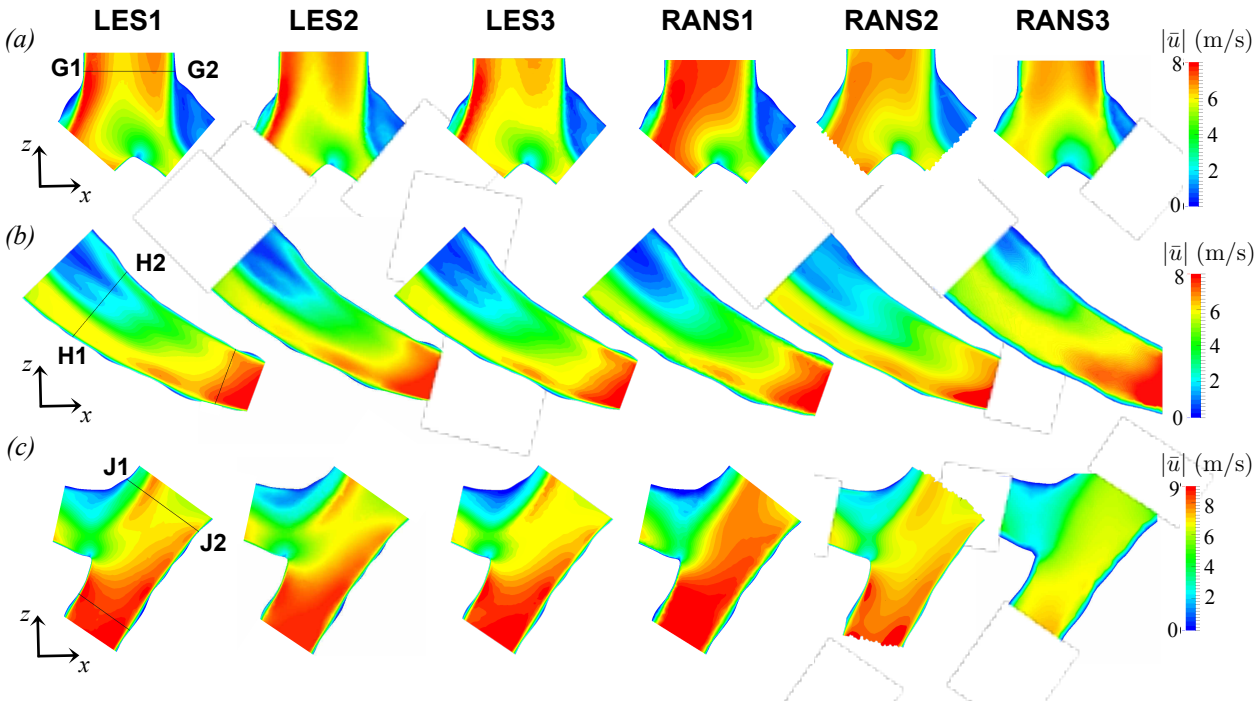

Figure 6: Contours of mean velocity magnitude in (*a*) the carina; (*b*) the left main bronchus; and (*c*) the right main bronchus.

Downstream of the trachea, the flow enters the bronchial tree. Contours of the mean velocity magnitude in the carina and main bronchi are shown in figure 6. The outlet conditions prescribed in the simulations, based on the flow distribution measured *in vitro*, result in high asymmetry in the ventilation of the two lungs, with the left lung receiving 29% of the inhaled air, and the right lung receiving 71%. This asymmetry is evident in the flow entering the tracheal bifurcation. A high-speed jet is observed along the right wall (G1-G2), and the stagnation point at the carina is offset towards the left. A larger recirculation region develops along the top wall of the left main bronchus (H1-H2), as it is at a more acute angle than the right. The asymmetry in the incoming flow and in the geometry, also results in higher velocities inside the right main bronchus.

Profiles of the mean velocity at the cross-sections displayed, are provided in figure 7. A slightly more skewed velocity profile at the entrance to the bifurcation (G1-G2, figure 7*a*) is obtained in simulation LES2, but otherwise very good agreement is observed across LES results. The largest differences occur in the recirculation region in the right main bronchus (J1-J2, figure 7*c*), since flow separation is particularly sensitive to mesh resolution and turbulence model. More noticeable differences in the mean flow profiles are observed in the RANS simulations. In general, the RANS models predict smoother velocity profiles, and have the most difficulty in predicting flow separation. As observed in the extrathoracic airways, the k-ω models (RANS1, RANS2) outperform the k-ϵ model (RANS3).

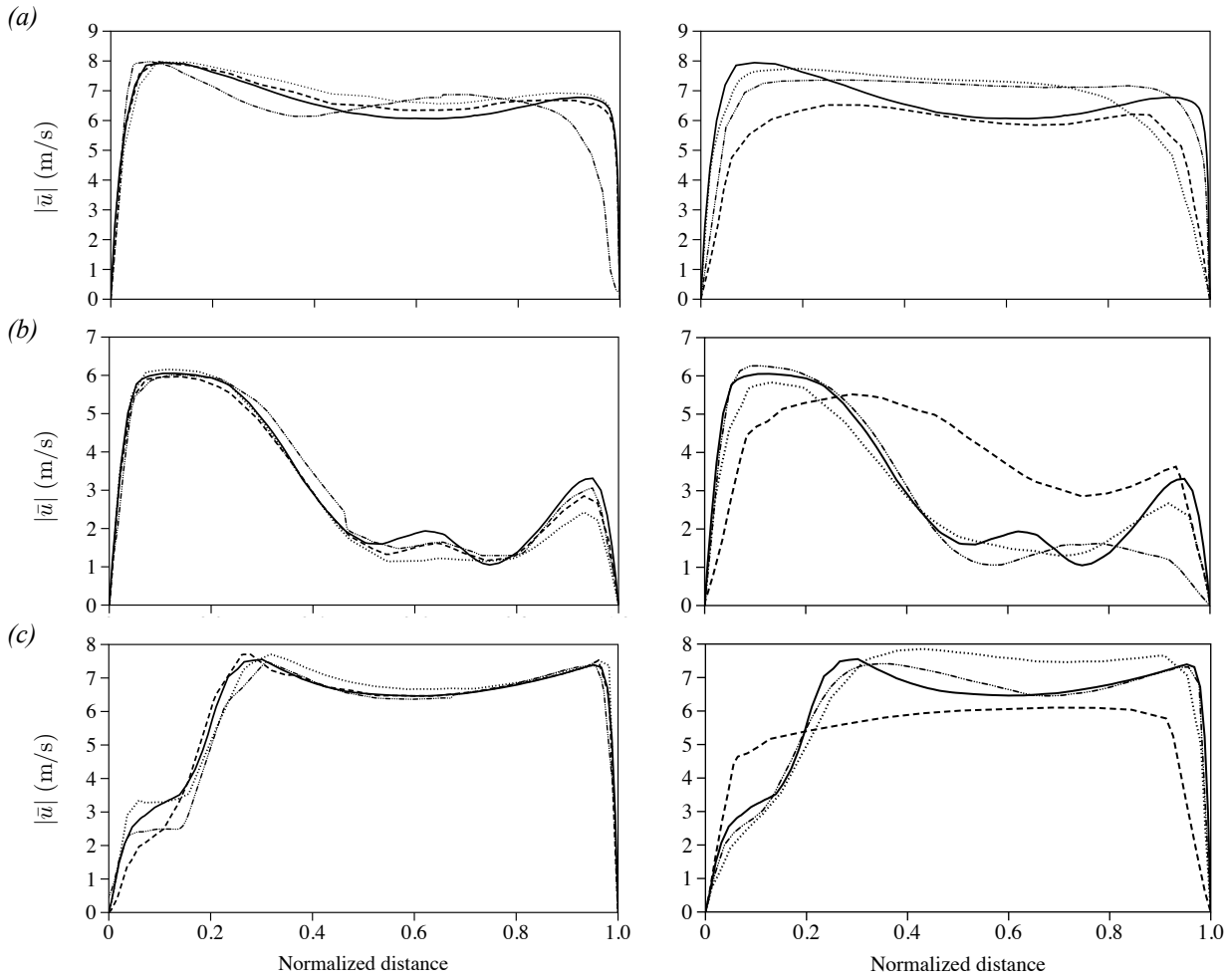

Figure 7: Profiles of mean velocity magnitude at cross-sections (*a*) G1-G2; (*b*) H1-H2; and (*c*) J1-J2. On the left: LES results, — LES1, ····· LES1c, -·-· LES2, - - - LES3. On the right: RANS results, — LES1, ····· RANS1, -·-· RANS2, - - - RANS3.

Predictions of the mean turbulent kinetic energy in the carina and main bronchi are shown in figure 8. Although turbulence levels appeared to decay in the trachea (figure 4*b*), high levels of k are observed here, in regions of high mean shear. The maximum kinetic energy occurs in the right main bronchus, between the separated shear layer and the recirculation region. New flow instabilities are induced at the bifurcation regions due to the severe geometric transition from the parent to the daughter branches, and result in high turbulence in the first few generations of the tracheobronchial tree (Kleinstreuer and Zhang, 2010). Good qualitative agreement is observed between LES1 and LES3, whereas LES1c and LES2 continue to underpredict turbulence levels. RANS1 performs poorly near regions of flow separation (figure 8*a*, *c*).

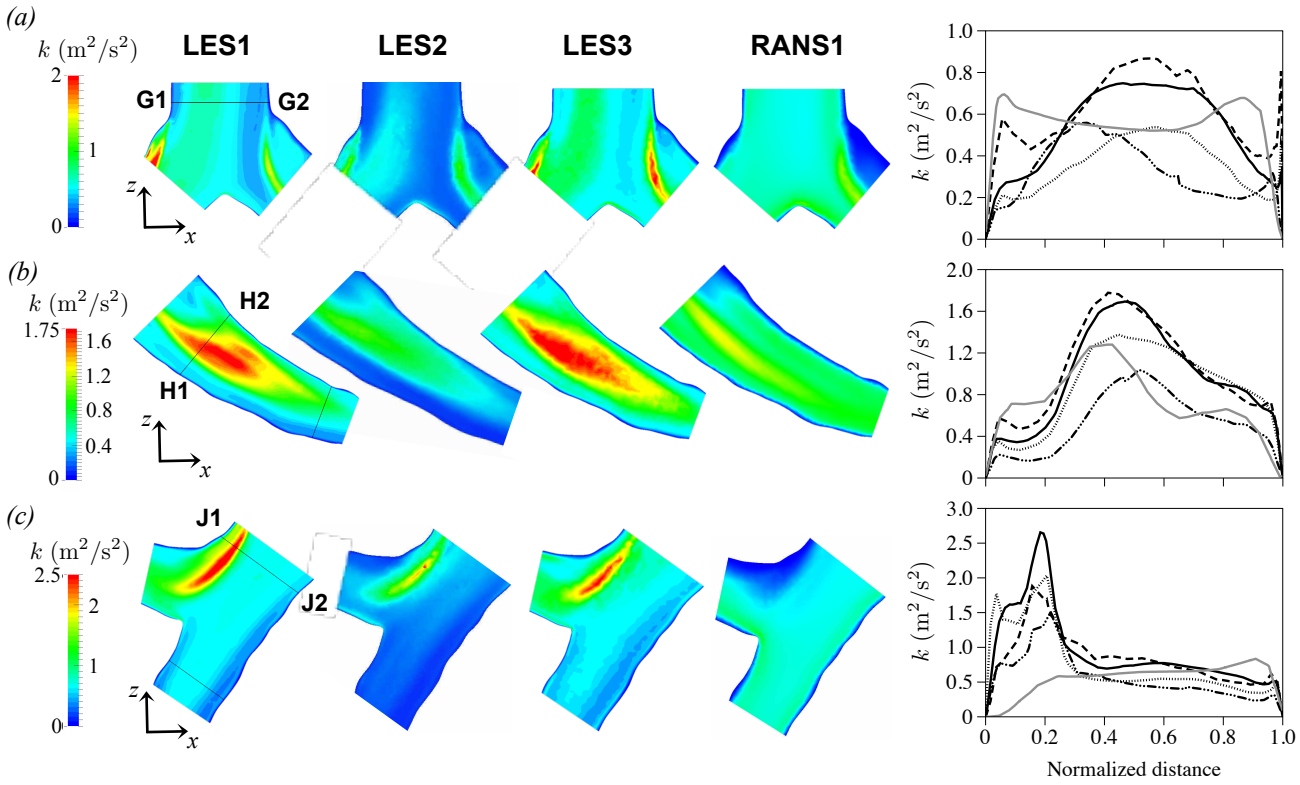

Figure 8: Contours and profiles of mean turbulent kinetic energy in (*a*) the carina; (*b*) the left main bronchus; and (*c*) the right main bronchus. — LES1, ····· LES1c, -·-·- LES2, - - - LES3, — RANS1.

Contours and profiles of the mean velocity in smaller airways of the bronchial tree are displayed in figures 9 and 10 respectively. As the left main bronchus narrows downstream, higher velocities are observed (figures 6*b*, 9*a*). The asymmetric branching results in a larger region of separation on the outer wall of the upper daughter branch. The airways are short, so the flow cannot develop fully. Due to upstream effects and different branching geometries, the flow varies significantly across the various bifurcations (figure 9*a-d*). In segment 7, for example, the flow enters the bifurcation with a large separation zone along the upper wall and a high-speed jet along the bottom, which leads to significant asymmetry in the flow distribution between daughter branches (figure 9*c*). Flow separation along the outer walls of the daughter branches is observed in most bifurcations, due to the relatively high local Reynolds numbers ($Re > 1000$) and abrupt increases in cross-sectional area.

Very good agreement between the LES simulations exists at all cross-sections. As observed upstream, the largest discrepancy generally occurs in regions of separation. Here, variability is greatest in the prediction of the extent of the recirculation zone at Y1-Y2 (figure 10*d*). Simulations

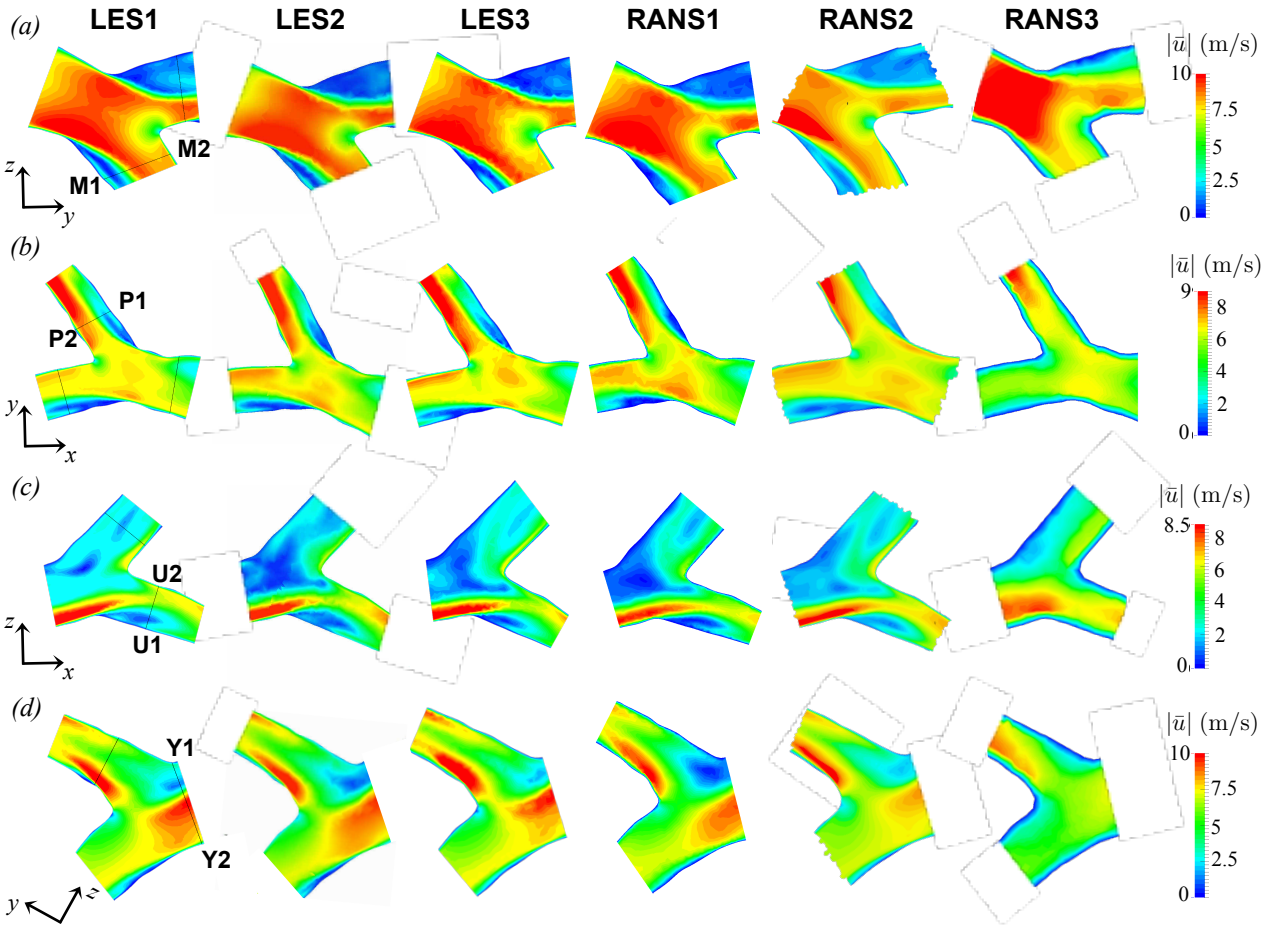

Figure 9: Contours of mean velocity magnitude in (*a*) segment 5 (left lung); (*b*) segment 9 (right lung); (*c*) segment 7 (left lung); and (*d*) segment 12 (right lung).

RANS1 and RANS2 are in reasonable agreement with the LES results, whereas RANS3 predicts a much more uniform flow field throughout. The low-*Re* k-ω model, RANS2, displays the best performance within the RANS simulations.

Finally, a comparison of the turbulent kinetic energy in the small airways, across the LES simulations and RANS1, is given in figure 11. Turbulent kinetic energy levels remain high in these airways which belong to generations 2 and 3. Turbulence has been observed to propagate to a few generations even at low local Reynolds number, due to the enhancement of flow instabilities at the bifurcations (Kleinstreuer and Zhang, 2010). Similar to the observations made upstream, the regions of maximum kinetic energy are in agreement across all LES simulations, however LES2 continues to underpredict overall turbulence levels. RANS1 is able to capture the turbulent kinetic energy with reasonable accuracy.

The comparison across simulations indicates that prediction of the flow in the upper airways is sensitive to mesh size and turbulence model, but less influenced by the inflow conditions. Flow transitions to turbulence at the back of the mouth, even when the inflow is laminar, and the effects of the inflow condition die out in the larynx. A larger variability is observed in the turbulent characteristics, compared to the mean flow field. A larger variation in deposition results is therefore expected for smaller particles that are more strongly influenced by the fluctuations in the flow. Across RANS simulations, the mean flow characteristics were captured best by the low-*Re* k-ω model. Simulations RANS2 and RANS3 were highly dissipative, and significantly underpredicted

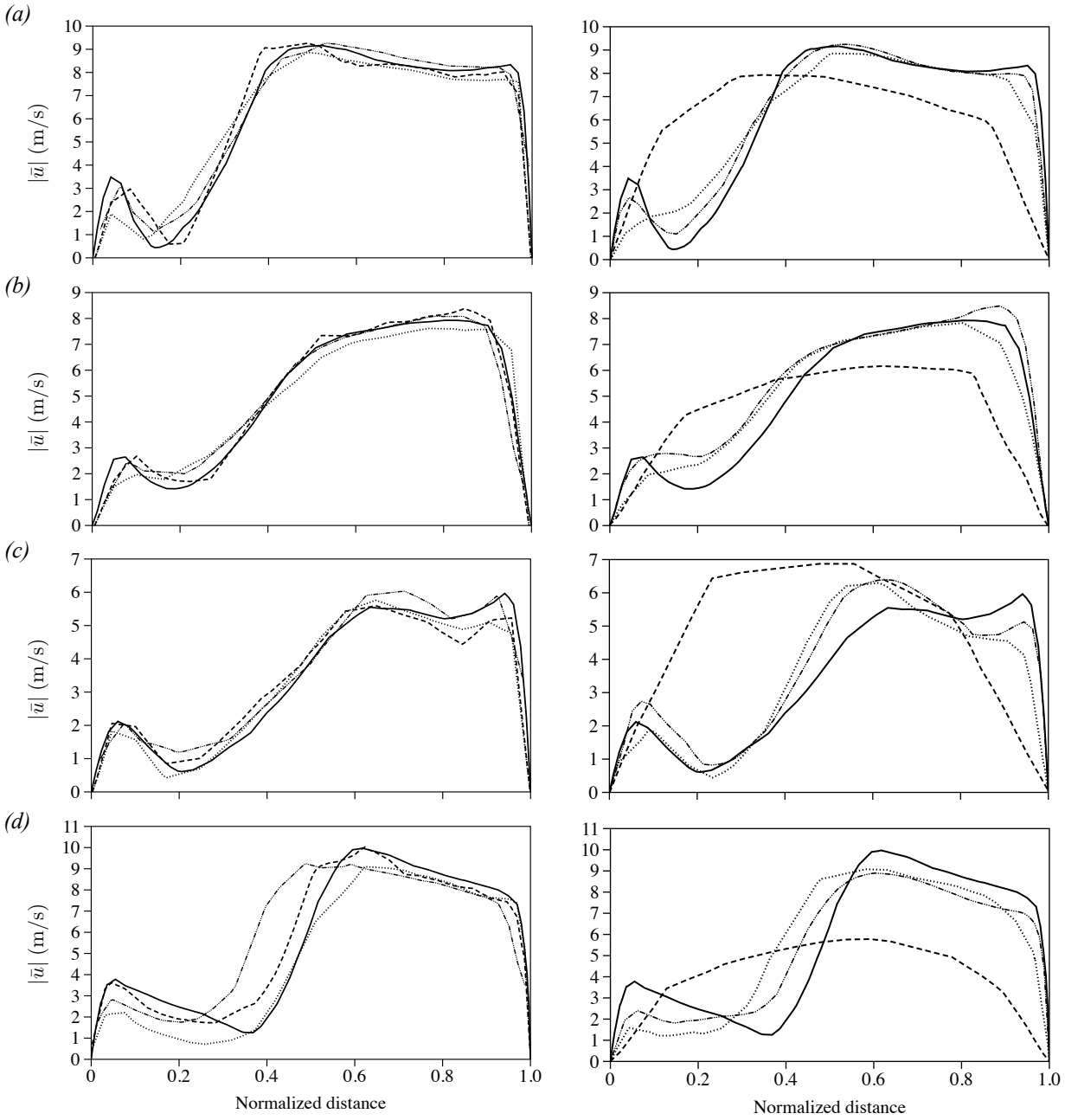

Figure 10: Profiles of mean velocity magnitude at cross-sections (*a*) M1-M2; (*b*) P1-P2; (*c*) U1-U2; and (*d*) Y1-Y2. On the left: LES results, — LES1, ····· LES1c, -·-· LES2, - - - LES3. On the right: RANS results, — LES1, ····· RANS1, -·-· RANS2, - - - RANS3.

turbulent kinetic energy in the airways, whereas RANS1 predicted overall turbulence levels with reasonable accuracy. Next, we turn to the aerosol particles, and examine how the variability in the flow field predictions affects regional deposition results.

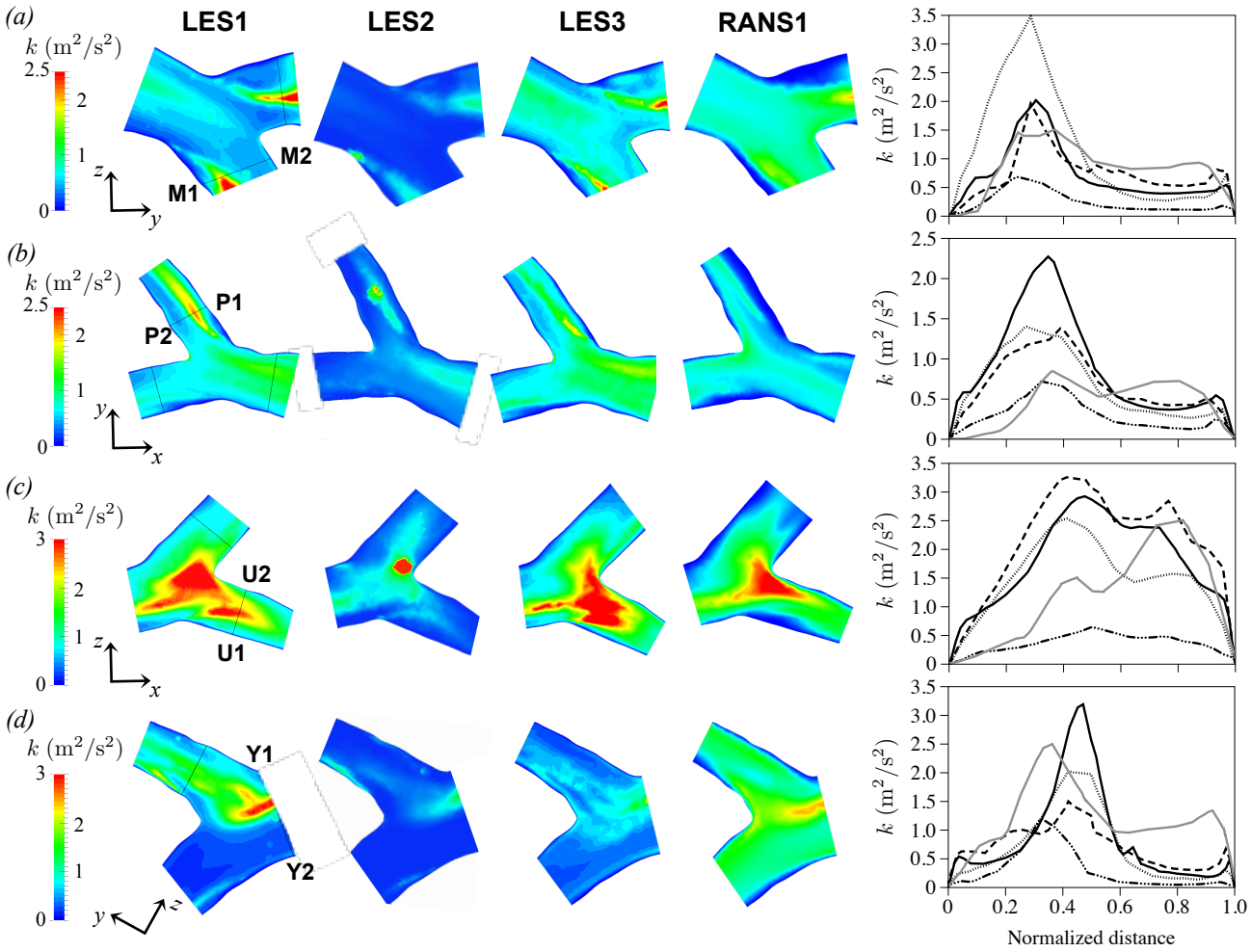

Figure 11: Contours and profiles of mean turbulent kinetic energy in (*a*) segment 5; (*b*) segment 9; (*c*) segment 7; and (*d*) segment 12. — LES1, ····· LES1c, -·-·- LES2, - - - LES3, — RANS1.

5.2. Aerosol deposition

In vitro measurements and numerical predictions of the aerosol deposition in the benchmark airway geometry are available on the SimInhale database for three flow rates, $Q = \{15, 30, 60\}$ L/min. Overall and regional deposition results are provided across a range of particle sizes for validation of CFPD methods. Here, we briefly examine the deposition at the three flow rates, before focusing on a comparison across the six numerical approaches at 60 L/min.

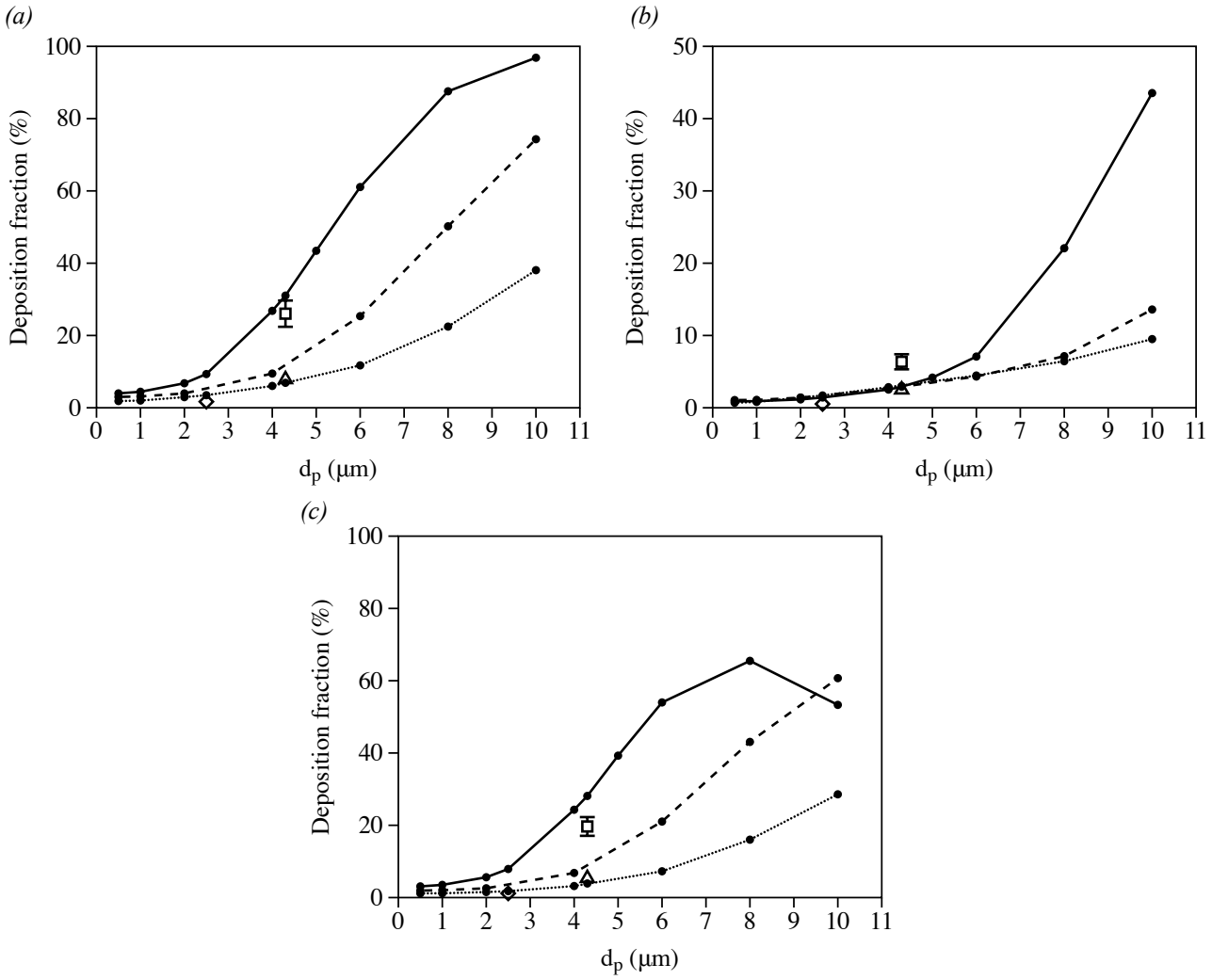

Figure 12: Deposition fractions at $Q = \{15, 30, 60\}$ L/min as a function of particle size in (*a*) the entire airway geometry; (*b*) the mouth-throat region; and (*c*) the tracheobronchial tree. Q = 15L/min: △ in vitro, ····· LES1; Q = 30L/min: ◇ in vitro, - - - LES1; Q = 60L/min: □ in vitro, — LES1.

Figure 12 shows deposition results from the *in vitro* experiments and the fine LES simulation for $Q = \{15, 30, 60\}$ L/min. Deposition fractions as a function of particle size in the entire geometry, mouth-throat region, and tracheobronchial tree are displayed in figures 12*a*, *b* and *c* respectively. Deposition increases with particle size for all three flowrates, suggesting that inertial impaction is the dominant deposition mechanism in the upper airways. The decrease in tracheobronchial deposition for 10μm particles at 60 L/min is a result of the significant filtering that occurs upstream in the mouth-throat region. An increase in overall and tracheobronchial deposition is also observed with increasing flow rate, and is more significant for the larger particles. In the extrathoracic region, deposition is largely unaffected by flow rate for particles smaller than 5

microns. These particles lie in the low Stokes number regime ($Stk < 0.01$), which is characterized by a weak dependence of deposition on Stokes number (Nicolaou and Zaki, 2016).

Good agreement is observed between numerical and experimental data at 15 and 30 L/min. In the high flow rate case, lower mouth-throat deposition is predicted in the LES. As a result of the reduced filtering in the mouth and throat, higher deposition is obtained in the tracheobronchial tree compared to the *in vitro* data. Underprediction of extrathoracic deposition by LES for high levels of turbulence has previously been reported in the literature, and can be attributed to the fact that the sub-grid scale influence on the motion of the particles is neglected in the particle-tracking scheme (Debhi, 2011). Additional sources of error could be related to experimental uncertainties, and differences in the particle distribution at the inlet between experiments and simulation.

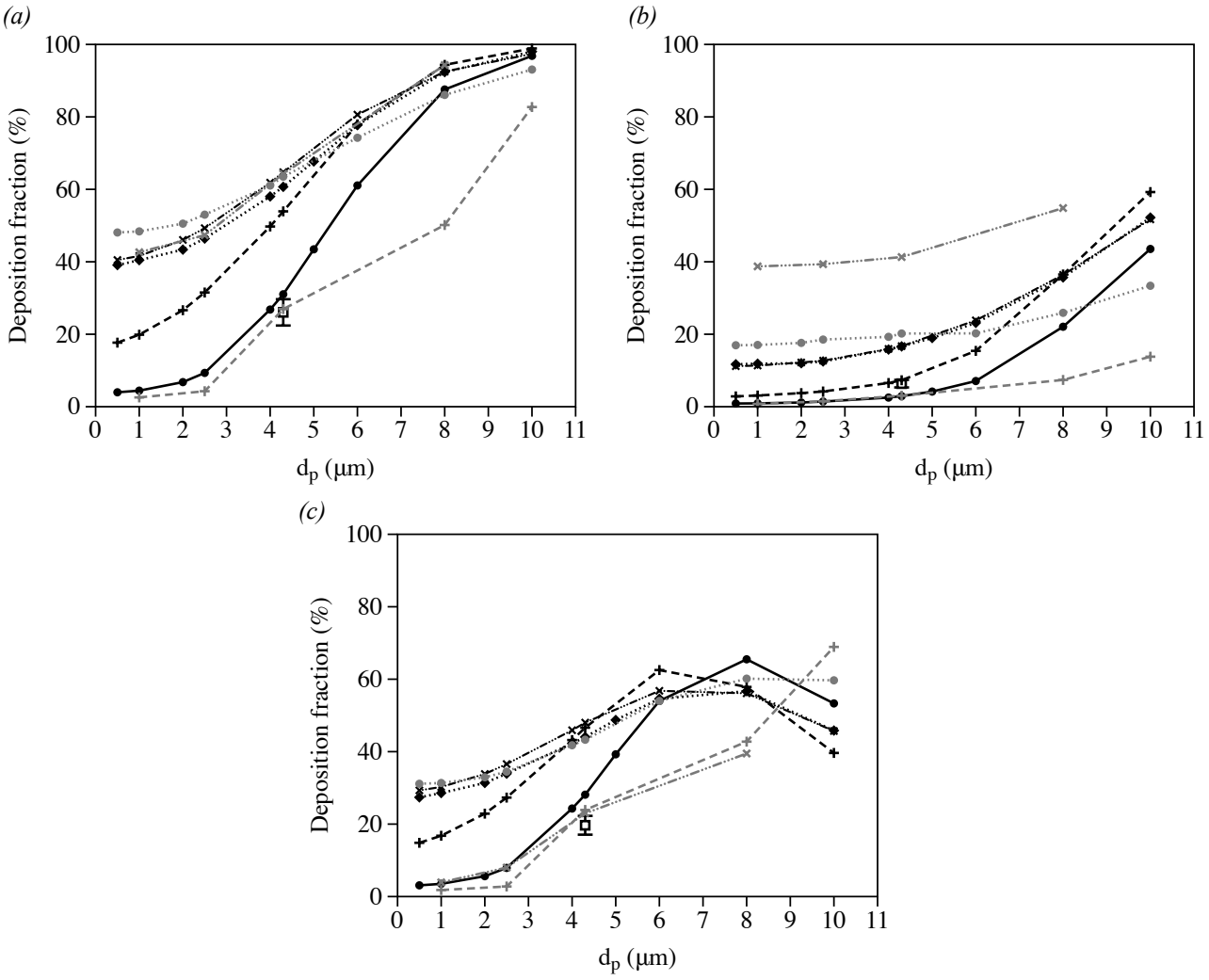

Figure 13: Deposition fraction as a function of particle size at Q = 60 L/min: (*a*) overall; (*b*) mouth and throat; and (*c*) tracheobronchial. □ *in vitro*, • LES1, ♦ LES1c, × LES2, + LES3, • RANS1, × RANS2, + RANS3.

A comparison of the deposition fractions predicted by the different simulation methods is shown in figure 13. Large variability can be seen in the overall deposition, which increases with decreasing particle size. Small particles are influenced by the velocity fluctuations, and are therefore particularly sensitive to errors in the flow field. Comparison of the predictions obtained in LES1 and LES1c shows that mesh size has a large effect on deposition. Interpolation errors in the particle-tracking scheme increase with decreasing grid resolution, and result in an overprediction

of deposition on the coarser mesh, in particular for the smaller particles. As in the mean flow and turbulent kinetic energy results, LES3 shows better agreement with the fine-grid LES simulation, compared to LES1c and LES2.

Within the RANS models, RANS1 and RANS2 overpredict extrathoracic deposition at small and intermediate particle sizes. In addition to interpolation errors, the disparity is likely due to an overprediction in the velocity fluctuations near the wall in the turbulent tracking schemes. Similar behaviour has been reported in the literature and has been improved by applying a near-wall correction to the velocity fluctuations (Matida et al., 2004; Jayaraju et al., 2008; Debhi, 2011). Simulation RANS3, on the other hand, adopted mean-flow tracking, which only accounts for impaction as a deposition mechanism, and does not include the effect of turbulent dispersion. This results in artificial good agreement with the fine LES simulation at small particle sizes, and considerable underprediction in deposition for the larger particles, particularly in the extrathoracic airways.

The deposition patterns in the extrathoracic airways, trachea and major bronchi are shown in figures 14 to 16, for particle sizes 1, 4.3 and 8 μm respectively. The same main deposition hotspots are observed across all three particle sizes. In the extrathoracic airways, major deposition occurs along the side walls of the pharynx. Additional hotspots are observed on the sharp step in the larynx, due to the sudden change in flow directions, and on the anterior wall slightly downstream, due to the separated shear layer. Some deposition also occurs in front of the tongue, where the incoming flow from the inlet pipe impinges.

In the trachea, very low deposition is observed for small particles. As particle size increases, deposition increases significantly. Particles deposit primarily along the upper half of the trachea, where the separated shear layer impinges on the anterior wall, and at the bend further downstream, where the high-speed velocity shifts from the anterior to the posterior wall (figure 4*a*). Downstream of the trachea, three main hotspots are observed: (i) just left of the carina, at the location of the stagnation point; (ii) along the upper wall of the right bronchus, due to the high-speed jet (figure 6*a*); and (iii) along the bottom wall of its daughter airway, as it branches off at a sharp angle.

In general, LES1 and LES3 predict similar deposition patterns. Interpolation errors in LES1c and LES2 cause higher deposition throughout the geometry, which results in a more uniform distribution, with less pronounced hotspots. RANS1 also displays high deposition, in particular along the posterior wall of the upper pharynx, and on the trachea walls. Sparser deposition is observed in RANS2, due to the small particle sample size employed. It is likely that the results are not statistically converged with 10,000 particles, and this could be the reason for the high extrathoracic deposition reported in figure 13*b*.

A more detailed comparison of the deposition results obtained in the LES simulations is shown in figure 17. Deposition fractions per segment of the airways are plotted for various particle sizes, in order to examine regional deposition. Segment numbers are shown in figure 2*c*. At small particle sizes, $d_p < 5\mu$m, overprediction is observed across the entire geometry in simulations LES1c, LES2 and LES3. For intermediate particles, $d_p = 6\mu$m, good agreement exists in the bronchial tree, whereas significant variability is observed in the mouth and throat. At this particle size, extrathoracic deposition has a strong dependence on Stokes number, and therefore a larger sensitivity to numerical errors. Tracheobronchial deposition on the other hand saturates around this particle size (figure 13*c*). Good agreement across LES predictions can be seen for the larger particles, $d_p = \{8, 10\}$ μm, as they are less sensitive to errors in the flow field and in the interpolation of the fluid velocity for the computation of the drag force (Lambert et al., 2011; Nicolaou and Zaki, 2016).

Figure 18 shows the regional depositions obtained in the RANS simulations. For small parti-

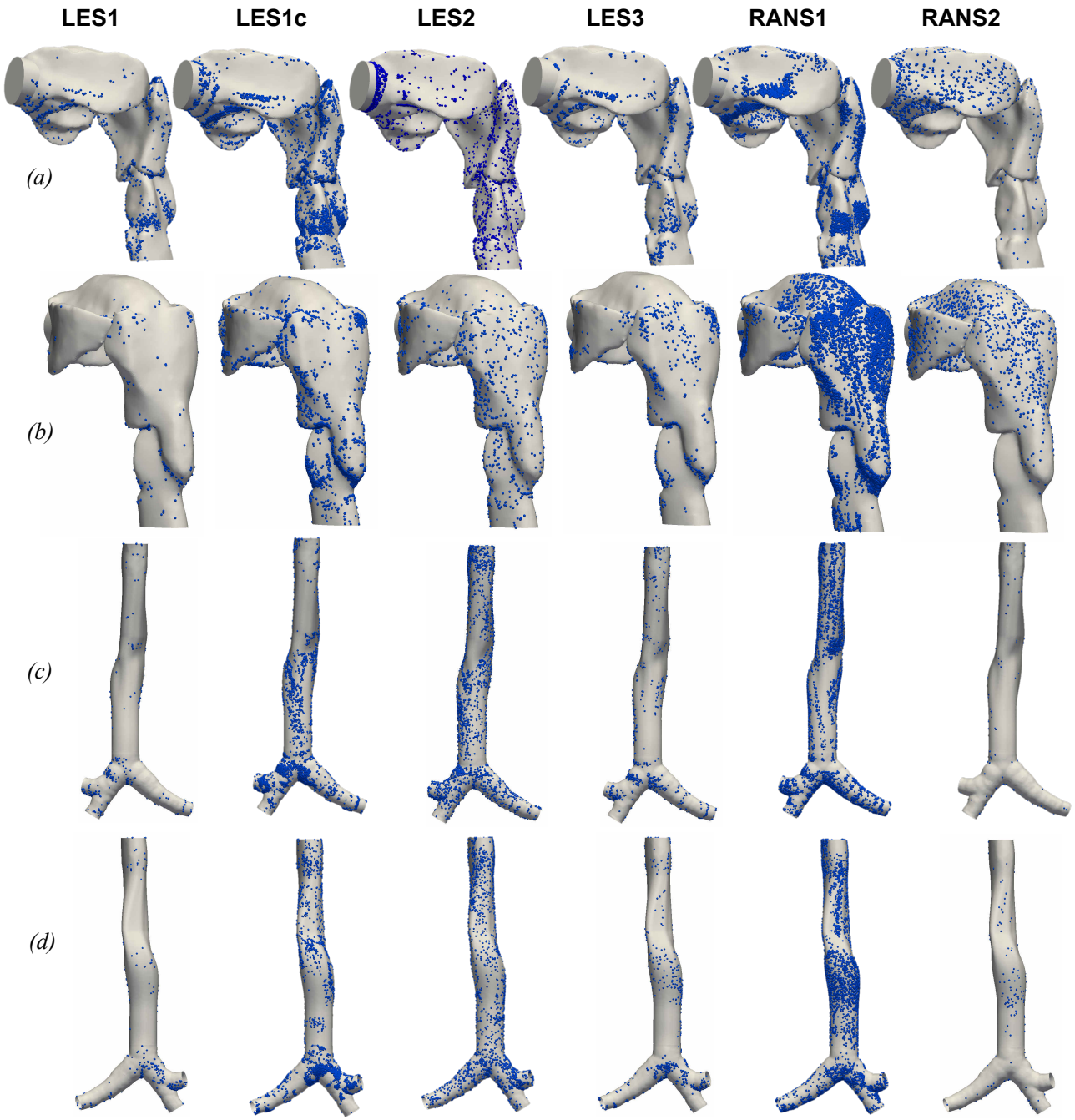

Figure 14: Deposition patterns for $d_p = 1$ µm: (*a*) sagittal and (*b*) posterior views of the extrathoracic airways; (*c*) anterior and (*d*) posterior views of the trachea and major bronchial airways.

cles, RANS3 is in good agreement with the fine-grid LES in the extrathroacic airways and trachea, and underpredicts deposition in the bronchial tree, as mean-flow tracking does not take into account turbulent dispersion. As particle size increases, this trend reverses, as extrathoracic and tracheal deposition are underpredicted, and a larger amount deposits in the bronchial regions due to the reduced filtering upstream. In RANS1, deposition is overpredicted across all segments for small particles, $d_p = 2.5$µm, and in the larger airways up to the main bronchi, for $d_p = 2.5$µm. At larger particle sizes, good agreement with the fine LES is observed in most segments, as particle trajectories become less sensitive to numerical errors. In simulation RANS2, overprediction oc-

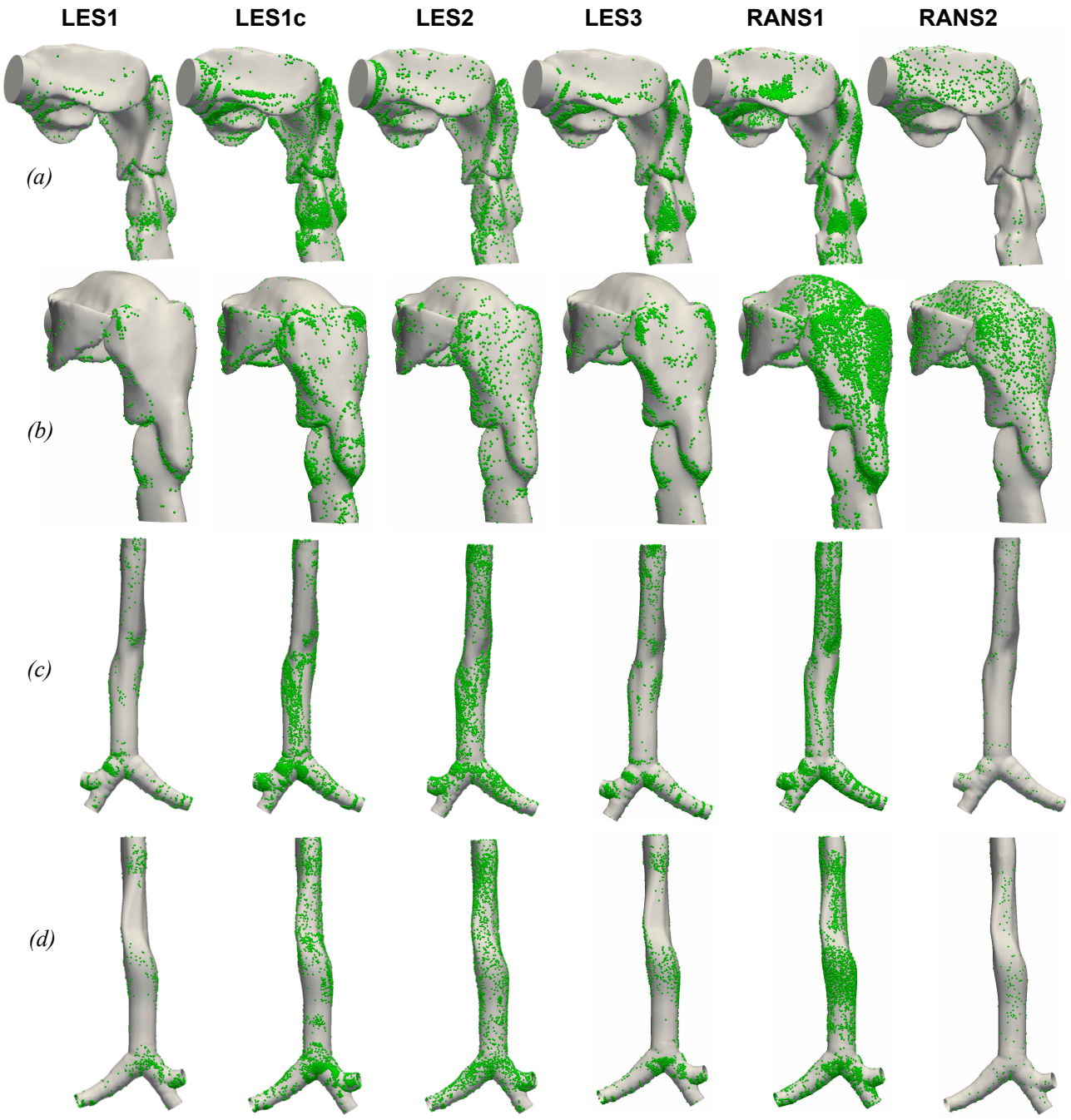

Figure 15: Deposition patterns for d_p = 4.3 µm: (*a*) sagittal and (*b*) posterior views of the extrathoracic airways; (*c*) anterior and (*d*) posterior views of the trachea and major bronchial airways.

curs primarily in the larger airways due to the small sample size, and extends further downstream as particle size decreases. At the smallest particle size, d_p = 2.5µm, deposition is significantly overpredicted in the extrathoracic airways (segment 1), the trachea (segment 2), and the left main bronchus (segment 4).

Finally, we briefly examine the effect of additional forces on deposition. Brownian motion was included in some of the simulations, but excluded in others. Its effect on the smallest particles, d_p = 0.5µm, is examined in figure 19*a*. The regional deposition results of RANS1, with and without Brownian force, show that Brownian motion has a negligible effect on deposition. Additional

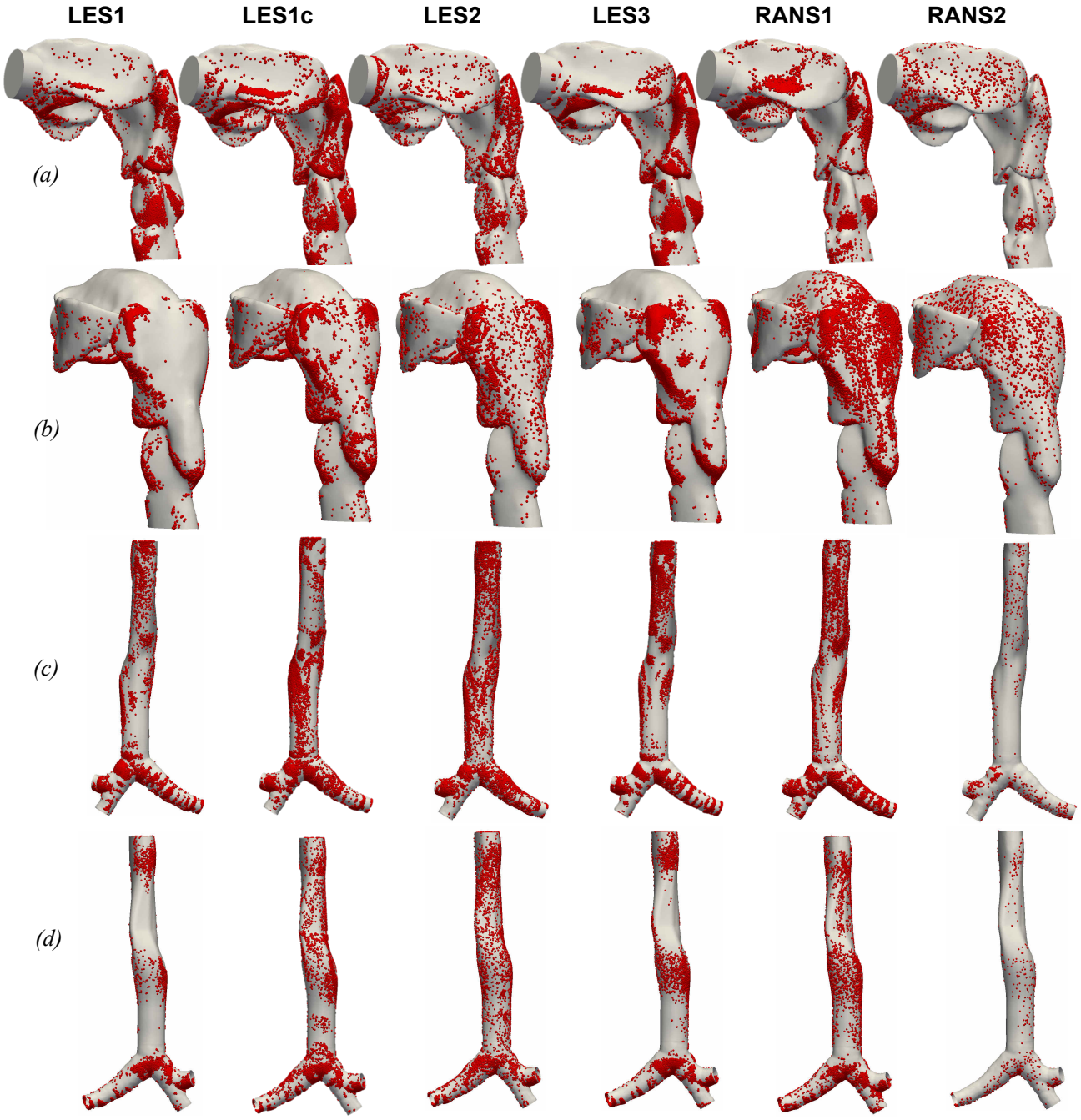

Figure 16: Deposition patterns for d_p = 8 µm: (*a*) sagittal and (*b*) posterior views of the extrathoracic airways; (*c*) anterior and (*d*) posterior views of the trachea and major bronchial airways.

forces, such as the pressure gradient and added mass, are typically considered negligible and were not taken into account in the simulations. However, for particles inside dry powder inhalers, transverse lift forces due to shear and rotation have been found to be significant (Sommerfeld and Schmalfuß, 2015; Sommerfeld, 2010). In figure 19*b*, the effect of transverse lift on particles inside the airways is considered for d_p = 4.3µm. The simulation taking into account only drag and gravity, and that including lift, yield negligible differences in regional deposition across the entire geometry. In the range of particle sizes studied, forces other than aerodynamic drag and gravity, have a marginal effect on deposition in RANS. In fine LES simulations, particles could potentially

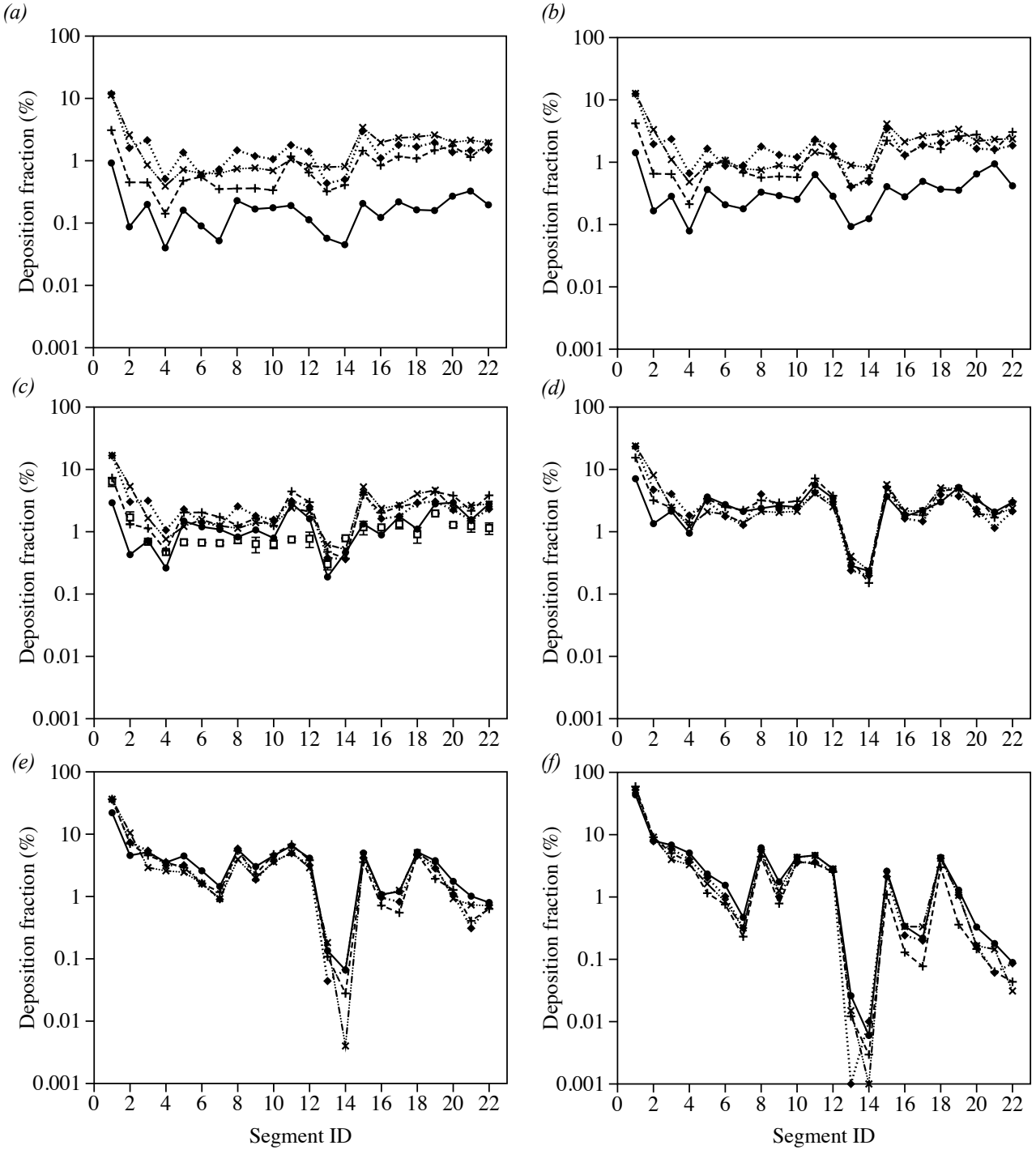

Figure 17: Deposition fractions in the various segments of the airway geometry, obtained from LES: (*a*) d_p = 1 µm; (*b*) d_p = 2.5 µm; (*c*) d_p = 4.3 µm; (*d*) d_p = 6 µm; (*e*) d_p = 8 µm; (*f*) d_p = 10 µm. □ *in vitro*, • LES1, ♦ LES1c, × LES2, + LES3.

exhibit larger sensitivity to lift, as the near-wall region, where Saffman lift is strongest, is better resolved.

570 A large variability in both global and regional deposition is observed across different computational approaches, especially in the low Stokes number regime. Deposition is particularly sensitive to mesh size and particle-tracking scheme, as interpolation errors increase with decreasing grid

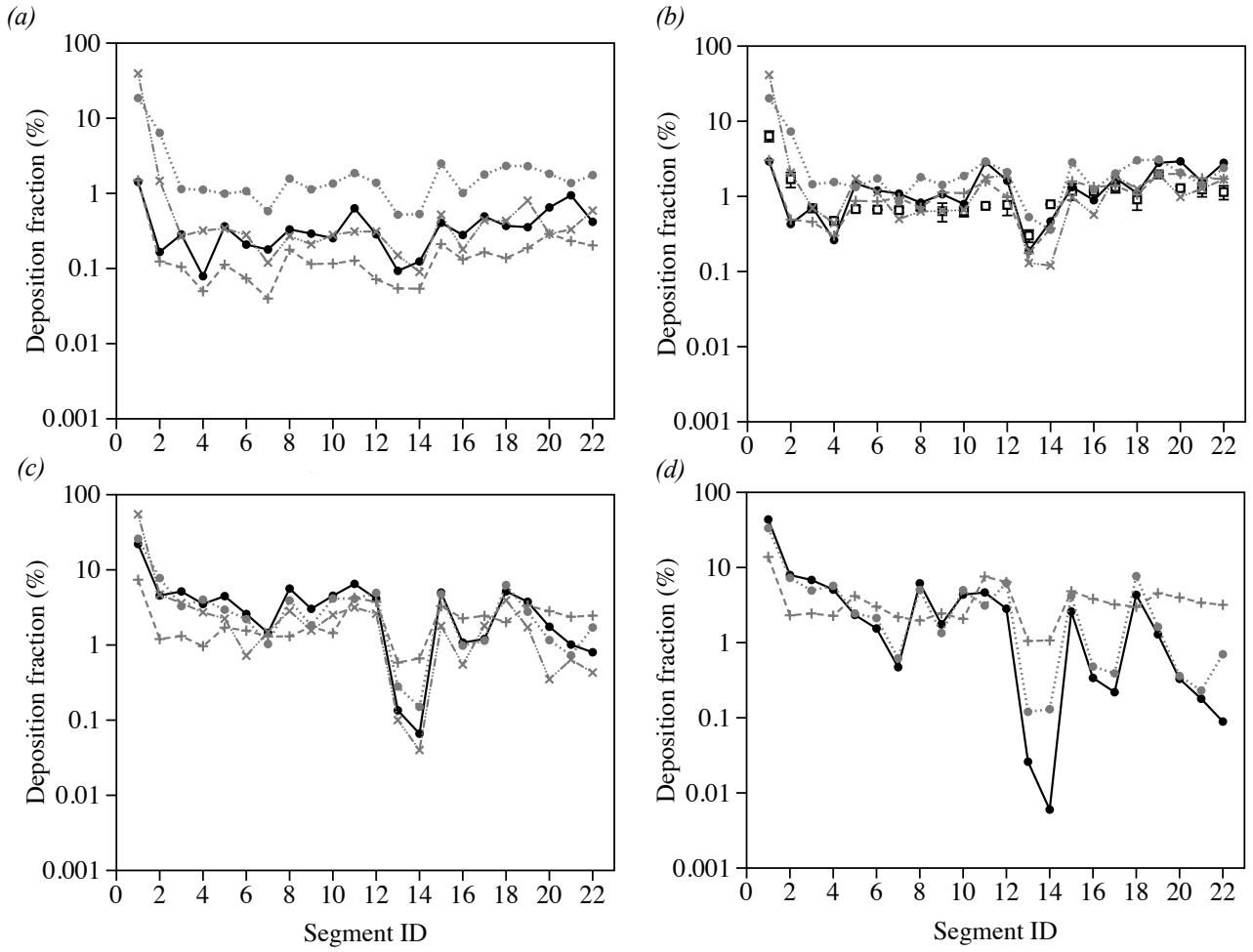

Figure 18: Deposition fractions in the various segments of the airway geometry, obtained from RANS: (*a*) d_p = 2.5 µm; (*b*) d_p = 4.3 µm; (*c*) d_p = 8 µm; (*d*) d_p = 10 µm. □ *in vitro*, • LES1, • RANS1, × RANS2, + RANS3.

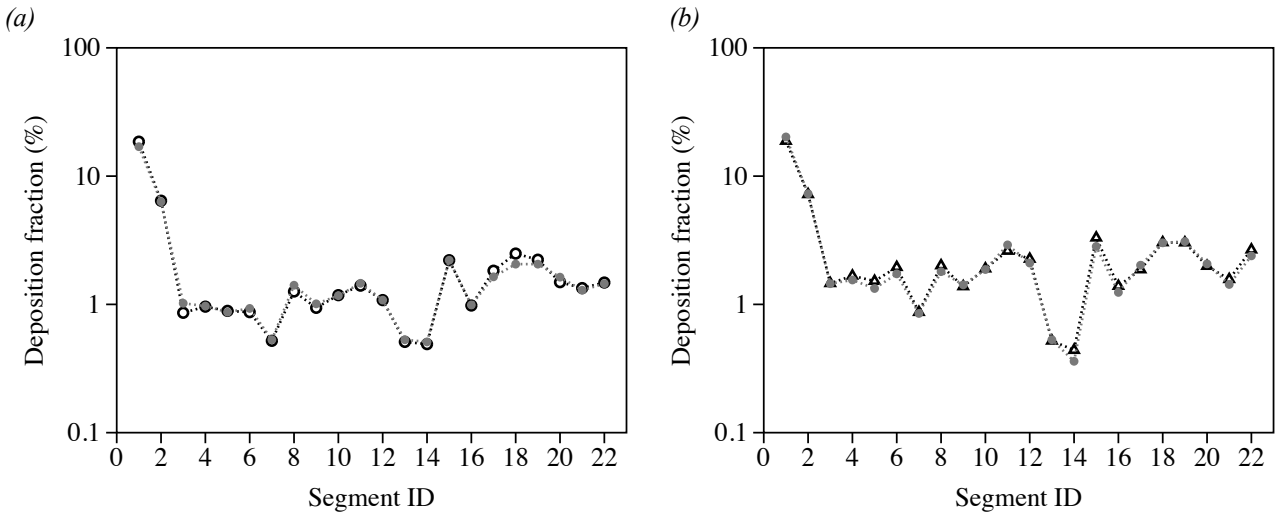

Figure 19: Deposition fractions in the various segments of the airway geometry, obtained in RANS1: (*a*) d_p = 0.5 µm; (*b*) d_p = 4.3 µm. • drag and gravity; ○ drag, gravity and Brownian force; △ drag, gravity and lift.

resolution and are heavily dependent on the scheme adopted. In addition, small particles are also affected by the accuracy in the turbulence statistics in LES, and the turbulent dispersion model in RANS, as their trajectories are significantly influenced by velocity fluctuations. In RANS, the effect of additional forces, such as Brownian motion and lift, has been found to be small for the range of particle sizes considered.

6. Conclusion

Regional deposition in the airways is important in the pulmonary delivery of drugs for topical treatment of respiratory diseases, as well as systemic delivery of drugs with limited lung bioavailability. Currently, *in vivo* studies remain limited by the spatial and temporal resolutions of imaging techniques, and by patient exposure to radiation. *In silico* methods offer a powerful tool to predict localized deposition in the airways, in order to further our understanding of the aerosol dynamics and optimize inhaled drug delivery. Numerical studies conducted to date have adopted a variety of computational techniques, a range of airway geometries varying in complexity, and differing assumptions on the flow and aerosol physics. A review of existing methods, with particular focus on the extrathoracic and upper conducting airways, was provided in Section 2.

One current limitation in the use of CFPD methods is the lack of detailed experimental data sets for validation of regional deposition results. Here, a benchmark case was presented, designed to serve as a reference for quality assurance of computational models in the upper airways. *In vitro* deposition measurements in a complex realistic geometry were provided at various inhalation flow rates, and six different simulation approaches were adopted to compute the benchmark case. Results were presented for the high flow rate, $Q = 60$ L/min, however *in silico* and *in vitro* data at $Q = \{15, 30\}$ L/min will also be published online and made available to the wider community.

To model the turbulent flow in the airways, three different large eddy simulation (LES) models and three Reynolds-averaged-Navier-Stokes (RANS) models were adopted. Different inflow conditions were applied across simulations, and mesh sizes ranged from 1.3 to 50 million grid cells. All simulations employed a Lagrangian particle-tracking approach and assumed one-way coupling between the flow and the particles. The approaches differed in the particle-tracking schemes adopted, the forces acting on the particles, and the release time and number of particles injected into the flow. In addition to serving as validation for CFPD methods, this benchmark case allowed us to examine the sensitivity of predictions to the numerical methods adopted, the mesh size, and the assumptions made in the modelling.

Prediction of the flow in the upper airways was found to be sensitive to mesh size and turbulence model, but less influenced by the inflow conditions. The flow transitions to turbulence at the back of the mouth, even when the inflow is laminar, and the effects of the inflow condition die out in the larynx. Generally, the mean flow fields obtained in the LES simulations were in good agreement. A larger variability was observed in the turbulent characteristics. Across RANS simulations, the mean-flow dynamics were captured best by the low-*Re* k-ω model on a mesh with prism layers near the wall. A higher-order scheme and turbulent inflow conditions in RANS1 resulted in turbulence levels comparable to LES, whereas RANS2 and RANS3 were too dissipative, and significantly underpredicted turbulent kinetic energy in the airways.

Significant variability in total and regional deposition results was seen across simulations. Deposition was found to be particularly sensitive to mesh size and particle-tracking scheme, especially at low Stokes numbers. Interpolation errors in the particle-tracking scheme increase with decreasing grid resolution, and are heavily dependent on the interpolation method adopted. Small particles are also influenced by the velocity fluctuations, and are therefore more sensitive to errors in the flow field. For larger particles, there was good agreement in regional deposition across LES

simulations. RANS with turbulent tracking overpredicted deposition at small and intermediate particle sizes, whereas mean-flow tracking significantly underpredicted deposition for larger particles. Forces other than drag and gravity were found to have a minor effect on the particles in RANS.

The airway model and the *in silico* and *in vitro* data presented in the manuscript, will be available online. PIV measurements of the flow in the benchmark case geometry will also be performed in future work, and additional numerical results will be appended to the online database as they become available. The aim is to provide a tool for the inhaled drug delivery community to (i) perform thorough validations of *in silico* models; and (ii) determine best practice guidelines for predictions of regional deposition in the airways, which can assist in the design and optimization of inhalation therapies.

Acknowledgements

This article is based upon work from COST Action MP1404 SimInhale 'Simulation and pharmaceutical technologies for advanced patient-tailored inhaled medicines', supported by COST (European Cooperation in Science and Technology) www.cost.eu. The work conducted at Brno University of Technology was partly supported by the Czech Science Foundation [16-23675S].

References

Balásházy, I., Hofmann, W., 1993. Particle deposition in airway bifurcations – I. inspiratory flow. Journal of Aerosol Science 24, 745–772.

Balásházy, I., Hofmann, W., Heistracher, T., 1999. Computation of local enhancement factors for the quantification of particle deposition patterns in airway bifurcations. Journal of Aerosol Science 30, 185–203.

Ball, C., Uddin, M., Pollard, A., 2008. Mean flow structures inside the human upper airway. Flow, Turbulence and Combustion 81, 155–188.

Cheng, K., Cheng, Y., Yeh, H.C., Swift, D.L., 1997. Measurements of airway dimensions and calculation of mass transfer characteristics of the human oral passage. Journal of Biomechanical Engineering-Transactions of the ASME 119, 476–482.

Choi, J., Tawhai, M.H., Hoffman, E.A., Lin, C.L., 2009. On intra- and inter subject variabilities of airflow in the human lungs. Physics of Fluids 21, 101901.

Cui, X., Gutheil, E., 2011. Large eddy simulation of the unsteady flow-field in an idealized human mouth-throat configuration. Journal of Biomechanics 44, 2768–2774.

Davies, C.N., 1945. Definitive equations for the fluid resistance of spheres. Proceedings of the Physical Society 57, 259.

Debhi, A., 2011. Prediction of extrathoracic aerosol deposition using RANS-random walk and LES approaches. Aerosol Science and Technology 45, 555–569.

DeHaan, W., Finlay, W., 2001. In vitro monodisperse aerosol deposition in a mouth and throat with six different inhalation devices. Journal of Aerosol Medicine 14, 361–367.

Dekker, E., 1961. Transition between laminar and turbulent flow in human trachea. Journal of Applied Physiology 16, 1060–1064.

Finlay, W., Stapleton, K., Yokota, J., 1996. On the use of computational fluid dynamics for simulating flow and particle deposition in the human respiratory tract. Journal of Aerosol Science 9, 329–341.

Ganser, G., 1993. A rational approach to drag prediction of spherical and nonspherical particles. Powder Technology 77, 143–152.

Gosman, A.D., Ioannides, E., 1983. Aspects of computer simulation of liquid fuelled combustors. Journal of Energy 7, 482–490.

Grgic, B., Finlay, W., Burnell, P., Heenan, A., 2004. In vitro intersubject and intrasubject deposition measurements in realistic mouth-throat geometries. Journal of Aerosol Science 35, 1025–1040.

Heenan, A., Matida, E., Pollard, A., Finlay, W., 2003. Experimental measurements and computational modeling of the flow filed in an idealized human oropharynx. Experiments in Fluids 35, 70–84.

Horsfield, K., Dart, G., Olson, D.E., Filley, G.F., Cumming, G., 1971. Models of the human bronchial tree. Journal of Applied Physiology 31, 207–217.

Houzeaux, G., Garcia, M., Cajas, J.C., Artigues, A., Olivares, E., Labarta, J., Vázquez, M., 2016. Dynamic load balance applied to particle transport in fluids. International Journal of Computational Fluid Dynamics 30, 408–418.

Hughes, T.J., Mazzei, L., Jansen, K.E., 2000. Large eddy simulation and the variational multiscale method. Computing and Visualization in Science 3, 47–59.

Jayaraju, S., Brouns, C., Lacor, C., Belkassem, B., Verbanck, S., 2008. Large eddy and detached eddy simulations of fluid flow and particle deposition in a human mouth–throat. Journal of Aerosol Science 39, 862–875.

Jayaraju, S.T., Brouns, M., Verbanck, S., Lacor, C., 2007. Fluid flow and particle deposition analysis in a realistic extrathoracic airway model using unstructured grids. Journal of Aerosol Science 38, 494–508.

Johnstone, A., Uddin, M., Pollard, A., Heenan, A., Finlay, W.H., 2004. The flow inside an idealised form of the human extra-thoracic airway. Experiments in Fluids 37, 673–689.

Kallio, G.A., Reeks, M.W., 1989. A numerical simulation of particle deposition in turbulent boundary layers. International Journal of Multiphase Flow 15, 433–446.

Kleinstreuer, C., Zhang, Z., 2003. Laminar-to-turbulent fluid-particle flows in a human airway model. International Journal of Multiphase Flow 29, 271–289.

Kleinstreuer, C., Zhang, Z., 2010. Airflow and particle transport in the human respiratory system. Annual Review of Fluid Mechanics 42, 301–334.

Koullapis, P.G., Kassinos, S.C., Bivolarova, M.P., Melikov, A.K., 2016. Particle deposition in a realistic geometry of the human conducting airways: Effects of inlet velocity profile, inhalation flowrate and electrostatic charge. Journal of Biomechanics 49, 2201–2212.

Lambert, A.R., O'shaughnessy, P.T., Tawhai, M.H., Hoffman, E.A., Lin, C.L., 2011. Regional deposition of particles in an image-based airway model: Large-eddy simulation and left-right lung ventilation asymmetry. Aerosol Science and Technology 45, 11–25.

Launder, B.E., Spalding, D.B., 1974. The numerical computation of turbulent flows. Computer methods in applied mechanics and engineering 3, 269–289.

Li, A., Ahmadi, G., 1992. Dispersion and deposition of spherical particles from point sources in a turbulent channel flow. Aerosol science and technology 16, 209–226.

Li, Z., Kleinstreuer, C., Zhang, Z., 2007. Particle deposition in the human tracheobronchial airways due to transient inspiratory flow patterns. Journal of Aerosol Science 38, 625–644.

Lilly, D., 1992. A proposed modification of the Germano subgrid-scale closure method. Physics of Fluids A: Fluid Dynamics 4, 633–635.

Lin, C.L., Tawhai, M.H., McLennan, G., Hoffman, E.A., 2007. Characteristics of the turbulent laryngeal jet and its effect on airflow in the human intra-thoracic airways. Respiratory Physiology & Neurobiology 157, 295–309.

Lizal, F., Belka, M., Adam, J., Jedelsky, J., Jicha, M., 2015. A method for in vitro regional aerosol deposition measurement in a model of the human tracheobronchial tree by the positron emission tomography. Proceedings of the Institution of Mechanical Engineers Part H-Journal of Engineering in Medicine 229, 750–757.

Lizal, F., Elcner, J., Hopke, P., Jedelsky, J., Jicha, M., 2012. Development of a realistic human airway model. Proceedings of the Institution of Mechanical Engineers Part H-Journal of Engineering in Medicine 226, 197–207.

Longest, P.W., Holbrook, L.T., 2012. In silico models of aerosol delivery to the respiratory tract – development and applications. Advanced Drug Delivery Reviews 64, 296–311.

Longest, P.W., Xi, J., 2008. Condensational growth may contribute to the enhanced deposition of cigarette smoke particles in the upper respiratory tract. Aerosol Science and Technology 42, 579–602.

Ma, B., Lutchen, K., 2009. Cfd simulation of aerosol deposition in an anatomically based human large–medium airway model. Annals of biomedical engineering 37, 271–285.

Matida, E., Finlay, W., Lange, C., Grgic, B., 2004. Improved numerical simulation of aerosol deposition in an idealized mouth-throat. Journal of Aerosol Science 35, 1–19.

Maxey, M.R., Riley, J.J., 1983. Equation of motion for a small rigid sphere in a nonuniform flow. Physics of Fluids 26, 883–889.

McLaughlin, J., 1989. Aerosol particle deposition in numerically simulated channel flow. Physics of Fluids A: Fluid Dynamics 1, 1211–1224.

Menter, F.R., 1994. Two-equation eddy-viscosity turbulence models for engineering applications. AIAA Journal 32, 1598–1605.

Morsi, S.A., Alexander, A.J., 1972. An investigation of particle trajectories in two-phase flow systems. Journal of Fluid Mechanics 55, 193–208.

Nicolaou, L., Jung, S.Y., Zaki, T.A., 2015. A robust direct-forcing immersed boundary method with enhanced stability for moving body problems in curvilinear coordinates. Computers & Fluids 119, 101–114.

Nicolaou, L., Zaki, T.A., 2013. Direct numerical simulations of flow in realistic mouth-throat geometries. Journal of

Aerosol Science 57, 71–87.
Nicolaou, L., Zaki, T.A., 2016. Characterization of aerosol Stokes number in 90° bends and idealized extrathoracic airways. Journal of Aerosol Science 102, 105–127.
Nicoud, F., Ducros, F., 1999. Subgrid-scale modelling based on the square of the velocity gradient tensor. Flow, Turbulence and Combustion 62, 183–200.
Oldham, M.J., 2000. Computational fluid dynamic predictions and experimental results for particle deposition in an airway model. Aerosol Science and Technology 32, 61–71.
Ounis, H., Ahmadi, G., McLaughlin, J., 1991. Brownian diffusion of submicrometer particles in the viscous sublayer. Journal of Colloid and Interface Science 143, 266–277.
Radhakrishnan, H., Kassinos, S., 2009. CFD modeling of turbulent flow and particle deposition in human lungs, in: Engineering in Medicine and Biology Society, EMBC 2009. Annual International Conference of the IEEE. pp. 2867–2870.
Schiller, L., Naumann, A., 1935. A drag coefficient correlation. VDI Zeitschrift 77, 318–320.
Schmidt, A., Zidowitz, S., Kriete, A., Denhard, T., Krassb, S., Peitgen, H.O., 2004. A digital reference model of the human bronchial tree. Computerized Medical Imaging and Graphics 28, 203–211.
Sommerfeld, M., 2010. Particle motion in fluids. VDI-Buch: VDI Heat Atlas, Part 11, 1181–1196.
Sommerfeld, M., Kohnen, G., Rüger, M., 1993. Some open questions and inconsistencies of lagrangian particle dispersion models, in: Ninth Symposium on Turbulent Shear Flows, Kyoto, Japan.
Sommerfeld, M., Schmalfuß, S., 2015. Numerical analysis of carrier particle motion in a dry powder inhaler. Journal of Fluids Engineering 138, 041308.
Stapleton, K.W., Guentsch, E., Hoskinon, M.K., Finlay, W.H., 2000. On the suitability of $k-\epsilon$ turbulence modeling for aerosol deposition in the mouth and throat: A comparison with experiment. Journal of Aerosol Science 31, 739–749.
Stylianou, F.S., Sznitman, J., Kassinos, S.C., 2016. Direct numerical simulation of particle laden flow in a human airway bifurcation model. International Journal of Heat and Fluid Flow 61, 677–710.
Tabor, G.R., Baba-Ahmadi, M.H., 2010. Inlet conditions for large eddy simulation: a review. Computers & Fluids 39, 553–567.
Thibodeau, G.A., Patton, K.T., 1996. Anatomy & physiology. 3rd ed., Mosby, St. Louis, MO.
Vázquez, M., Houzeaux, G., Koric, S., Artigues, A., Aguado-Sierra, J., Arís, R., Mira, D., Calmet, H., Cucchietti, F., Owen, H., et al., 2016. Alya: Multiphysics engineering simulation toward exascale. Journal of Computational Science 14, 15–27.
Weibel, E.R., 1963. Morphometry of the human lung. Berlin-Academic Press.
Xi, J., Longest, W., 2007. Transport and deposition of micro-aerosols in realistic and simplified models of the oral airway. Annals of Biomedical Engineering 35, 560–581.
Yeh, H.C., Schum, G., 1980. Models of human lung airways and their application to inhaled particle deposition. Bulletin of Mathematical Biology 42, 461–480.
Young, J., Leeming, A., 1997. A theory of particle deposition in turbulent pipe flow. Journal of Fluid Mechanics 340, 129–159.
Zhang, Z., Kleinstreuer, C., Kim, C.S., 2002. Micro-particle transport and deposition in a human airway model. Journal of Aerosol Science 33, 1635–1652.
Zhang, Z., Kleinstreuer, C., Kim, C.S., Cheng, Y.S., 2004. Vaporizing microdroplet inhalation, transport, and deposition in a human upper airway model. Aerosol Science and Technology 38, 36–49.